INL/JOU-24-79826-Revision-0

Critical Review of LPBF Metal Print Defects Detection: Roles of Selective Sensing Technology

August 2024

Donna Post Guillen, Scott Wahlquist, Amir Ali

Changing the World's Energy Future

Idaho National Laboratory

INL/JOU-24-79826-Revision-0

Critical Review of LPBF Metal Print Defects Detection: Roles of Selective Sensing Technology

Donna Post Guillen, Scott Wahlquist, Amir Ali

August 2024

Idaho National Laboratory
Idaho Falls, Idaho 83415

http://www.inl.gov

Prepared for the
U.S. Department of Energy
Under DOE Idaho Operations Office
Contract DE-AC07-05ID14517

applied sciences

MDPI

Review

Critical Review of LPBF Metal Print Defects Detection: Roles of Selective Sensing Technology

Donna Guillen [1], Scott Wahlquist [2] and Amir Ali [2,3,*]

[1] Idaho National Laboratory, Idaho Falls, ID 83415, USA; donna.guillen@inl.gov
[2] Department of Nuclear Engineering, Collage of Science and Engineering, Idaho State University, Pocatello, ID 83209, USA; scottwahlquist@isu.edu
[3] Center for Advanced Energy Studies, Idaho Falls, ID 83401, USA
* Correspondence: aliamir@isu.edu; Tel.: +1-208-533-8108

Abstract: The integrative potential of LPBF-printed parts for various innovative applications depends upon the robustness and infallibility of the part quality. Eliminating or sufficiently reducing factors contributing to the formation of defects is an integral step to achieving satisfiable part quality. Significant research efforts have been conducted to understand and quantify the triggers and origins of LPBF defects by investigating the material properties and process parameters for LPBF-printed geometries using various sensing technologies and techniques. Frequently, combinations of sensing techniques are applied to deepen the understanding of the investigated phenomena. The main objectives of this review are to cover the roles of selective sensing technologies by (1) providing a summary of LPBF metal print defects and their corresponding causes, (2) informing readers of the vast number and types of technologies and methodologies available to detect defects in LPBF-printed parts, and (3) equipping readers with publications geared towards defect detection using combinations of sensing technologies. Due to the large pool of developed sensing technology in the last few years for LPBF-printed parts that may be designed for targeting a specific defect in metal alloys, the article herein focuses on sensing technology that is common and applicable to most common defects and has been utilized in characterization for an extended period with proven efficiency and applicability to LPBF metal parts defect detection.

Keywords: additive manufacturing; laser powder bed fusion (LPBF); defect classification; defect detection; sensing technologies

Citation: Guillen, D.; Wahlquist, S.; Ali, A. Critical Review of LPBF Metal Print Defects Detection: Roles of Selective Sensing Technology. *Appl. Sci.* **2024**, *14*, 6718. https://doi.org/10.3390/app14156718

Received: 14 June 2024
Revised: 15 July 2024
Accepted: 21 July 2024
Published: 1 August 2024

1. Introduction

Additive manufacturing (AM) is the fabrication process of generating precise geometrical shapes through the sequential deposition of incremental layers. The application range of AM is incredibly vast and continues to garner increased industry attention due to its rapid prototyping potential. It offers flexible design freedom, short lead times, and reliable manufacturability of dense parts. AM of metals is accomplished by fully melting either powder or wire feedstock using the energy input from a laser or electron beam. The energy strategically lays the melted metal in a specific configuration for the current layer. The deposition of each layer is repeated until the physical part is completed. The various AM methodologies can be taxonomized by the binding mechanism(s) between the joined layers of material and the aggregate state and nature of the feedstock material composition. Metal AM binding mechanisms can be classified into three main processes: laser beam melting (LBM), electron beam melting (EBM), and laser metal deposition (LMD). Other names for the LBM process include laser powder bed fusion (LPBF), selective laser melting (SLM), direct metal laser sintering (DMLS), and laser metal fusion [1]. The LBM and EBM methods are powder bed-based processes, where the product is developed by melting metal powder layer by layer using a high-performance laser (LBM) and electron beam gun (EBM). The

powder bed platform is lowered after each layer of exposure to create vertical space for the new layer of powder. LBM operates in a protective inert gas chamber environment, while EBM operates under vacuum conditions. The LMD process applies metal powder through a nozzle while simultaneously melting the feedstock using a laser. In LMD processes, the deposition heat is typically repositioned for each layer while the part is kept stationary. A stationary deposition head and moving base plate have also been proven to work.

The proof-of-concept for each AM process has been established, though some technologies have been more popular than others, including LPBF. For the LPBF printing process, the metal powder substrate is deposited from an industrial hopper or an adjacent powder supply and smoothed using a leveling system to achieve a uniform distribution. Once the scan has been completed for the current height, the build plate is slightly lowered, and the next layer is deposited and smoothed. This process is repeated until the part is completed. The laser beam sources for all current LPBF technologies are ytterbium or Nd-YAG fiber lasers with a power range between 200 and 1000 W that can generate a laser spot diameter range between 50 and 100 μm [2]. The variability of other parameters, such as scan speed, hatch spacing, and layer thickness, usually depends on the particular machine's limitations.

Though the LPBF process can produce highly accurate and complex parts, it is not immune to defects. The types of defects can be mainly attributed to the material's (thermophysical and microstructural) properties and the manufacturing process parameters. Theoretically, combining optimized process parameters and appropriate material properties should provide synergistic conditions to produce parts with no defects. In reality, however, the appropriate conditions for a one-part build may be unacceptable for another, producing unforeseen defects not observed in prior prints. Significant research efforts have been reported to understand and quantify the triggers and origins of LPBF defects by investigating the material properties and process parameters for various geometries. These investigations into defect detection and monitoring are accomplished through three primary sources: sensing technologies (optical, thermal, acoustic, and ultrasonic), numerical methods (finite element, finite volume, analytical coding), and the integration of artificial intelligence (AI) models (supervised, unsupervised, and semi-supervised).

The goals of this review article are to cover the roles of sensing technologies by (1) providing a summary of LPBF metal print defects and their corresponding causes, (2) informing readers of the vast number and types of technologies and methodologies available to detect defects in LPBF-printed parts, and (3) equipping readers with publications geared towards defect detection using combinations of sensing technologies.

2. Classification of LPBF Defects

The LPBF printing process has a high probability that something can go wrong, despite the process being considered thoroughly optimized. There is no such printed LPBF part that is perfectly free of flaws. The complexity of the LPBF printing process counters many inherent phenomena that are not fully understood. Massive research efforts have been reported to understand these phenomena and eliminate or reduce defect probabilities. The standard approach to mitigating defects is to evaluate and reevaluate the process parameters and/or material compositions based on the data collected in situ and post-processing techniques. The generally reported defects are divided into four separate categories: (1) geometrical/dimensional defects, (2) surface-quality defects, (3) microstructure defects, and (4) mechanical defects. Many of these presented defects can be considered interrelated or even interdependent.

2.1. Geometrical/Dimensional Defects

Geometrical and dimensional defects can be attributed to either user and/or machine errors. User errors are typically resolved as the user becomes accustomed to LPBF technology. However, machine errors are often inevitable, though some can be reduced.

User errors include (1) unoptimized manual input process parameters, (2) improper machine configuration setup and preparation, and (3) faulty usage of support structures.

Unoptimized manually input process parameters are those process parameters (i.e., laser power, hatch spacing, scan speed) that the user can directly control. Certain part defects can occur throughout the build by choosing improper process parameters. Improper machine configuration setup and preparation can include not inspecting the recoater blade and not correctly resetting the build plate. A common improper preparation step is exposing the powder particles to atmospheric conditions, which leads to oxidation [3].

Machine errors include (1) insufficient resolution error, (2) laser positioning/intensity error, and (3) platform-movement error. The staircase effect is one of the main resolution errors contributing to dimensional defects. It is defined as a stepped approximation by layers of curved and inclined surfaces due to limited fabrication resolution [4]. Insufficient resolution can cause higher surface roughness for curved surfaces. Laser positioning errors are due to slight shifts of the laser beam before or during the build process. Laser intensity errors occur when the adjusted laser intensity does not match the actual intensity. Both laser positioning and intensity errors are often associated with the software and machinery. Similarly, platform-movement errors are caused by a defective motion in the vertical direction, preventing even recoating and causing damage to the recoater blade.

2.2. Surface-Quality Defects

Surface-quality defects pertain to defects that appear on the end surface of the part or the current scan's surface. Surface-quality defects are often an indication of more severe defects present within the part. The surface-quality defects include balling, surface roughness, surface oxidation, denudation, and vaporization.

Balling results from insufficient wettability occurring during the deposition of the melt track and can lead to pores, higher surface roughness, and irregular melt tracks [5]. Balling occurs due to the combination of surface tension and capillary forces that drive the melt pool to shrink to its lower surface energy state. Poor contact with the underlying substrate causes spheroidic or ellipsoidal ball-shaped structures to form [6]. The balling phenomenon can be mainly attributed to the process parameters (i.e., laser power, scan velocity, hatch spacing, layer thickness) and the physical properties of the substrate material. The main properties contributing to balling initiation are the high surface tension and viscosity. Higher laser power induces more heat to form, decreasing the viscosity and increasing the wettability of the molten melt pool. Severe oxidation has also been observed to exacerbate wetting capabilities [7]. In extreme cases, balling can potentially obstruct the deposition process through the formation of humps and ripples on the surface. These humps and ripples are further accentuated as subsequent layers are stacked. They can potentially damage the recoater and lead to costly and time-consuming maintenance. Figure 1 displays the balling of the sintered AlSi10Mg powder at various scan speeds [8].

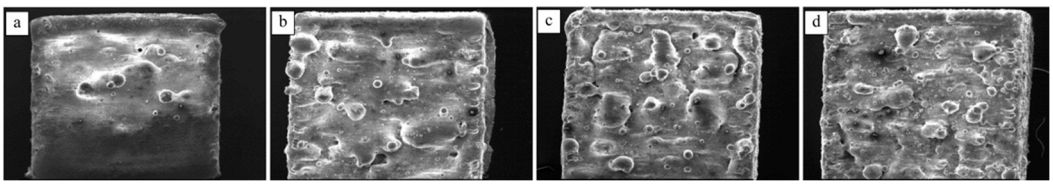

Figure 1. The severity of the balling phenomena increases as the scan speed increases, as shown by the LPBF printed surface profiles with scan speeds of (**a**) 250 mm/s, (**b**) 500 mm/s, (**c**) 750 mm/s and (**d**) 1000 mm/s (modified from [8]).

Surface oxidation occurs when oxygen is present. Oxidation is a significant problem for alloys containing Si or Mg [9]. Even though most LPBF processes are performed under protective environments with a shielding inert gas flow, a small percentage of unwanted oxygen content (~0.1–0.2%) can be present [10]. Oxygen is often found in the fillings between the powder particles. Over time, passive oxide films can be formed on the powder's surface, immediately affecting the scan quality. The thickness of the oxide

film layer is vital in that nm thick oxide films can cause negligible damage, while µm thick oxide films (10–100 µm) can cause irregular geometries to form [9].

In the presence of oxide films, the film is broken up during laser re-melting, causing some oxide particles to solidify underneath the surface while others float to the surface and form a new oxide layer. As subsequently deposited oxide layers are stacked over each other, porosities can form, which can cause cracking and weak mechanical properties. Clean and dried powders are recommended to reduce surface oxidation. Figure 2 highlights the effects of slight and severe oxidation on the surface quality of processed SS316L.

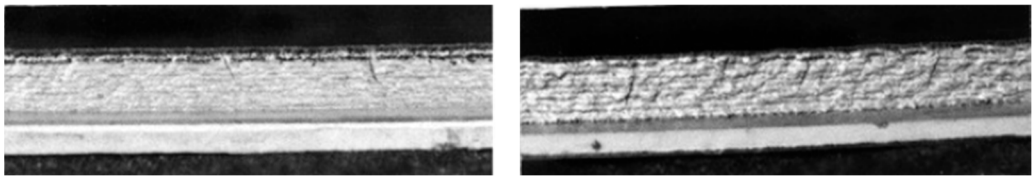

Figure 2. Oxidation effects of SS316L surface quality, slight oxidation (**left**), and severe oxidation (**right**) [11].

Surface roughness severity depends upon many factors, including process parameters (laser power, scan velocity, layer thickness, and hatch spacing). The surface quality is affected by two main behaviors, namely oxidation and powder adhesion on the surface [11]. Surface oxidation causes an oxide film, affecting the subsequent layers' adhesion to the surface. Process parameters directly affect the powder adhesion effectiveness and, in turn, the part surface roughness. For example, increasing the laser scanning velocity decreases the formation time of the melt pool length, which resultantly decreases the width of the melt pool. It encourages the melt pool to break down into an uneven surface during the current scan, leading to higher surface roughness for subsequent scans. The surface roughness can decrease by providing higher energy density, laser power at lower speeds, and adequate hatch spacing [12]. Figure 3 displays the surface roughness profile of a 17-4 PH SS LPBF-printed part [13].

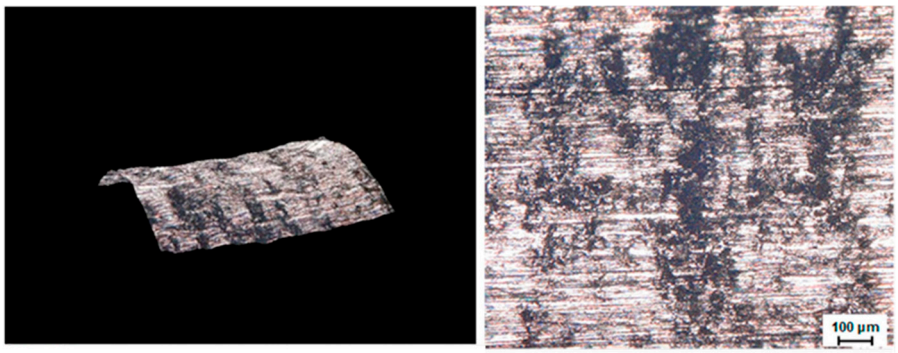

Figure 3. Characterized surface roughness profile of LPBF 17-4 PH SS specimens [13].

Denudation occurs when the powder particles around the solidified melt track are depleted. Denudation has been reported to cause porosities and high surface roughness from accumulating un-melted or partially melted particles between the layers [14]. Increased laser power, scan speeds, and environmental gas pressure can cause a decrease in pressure inside the vapor plume. The low pressure favors ambient gas flow towards the center of the melt track. The gas flow is powerful enough to sweep powder particles along its flow. These particles can be incorporated into the melt pool or ejected with the vapor plume [15]. Powder denudation can also occur when insufficient laser power completely melts the powder. The surface tension of the powder substrate enables partially melted particles to go back into the melt pool, depleting the powder around the melt track. Careful selection of the hatch spacing is recommended to avoid denudation [16]. Figure 4 highlights the effects of laser power on the denudation zone width for Ti6Al4V powder [15].

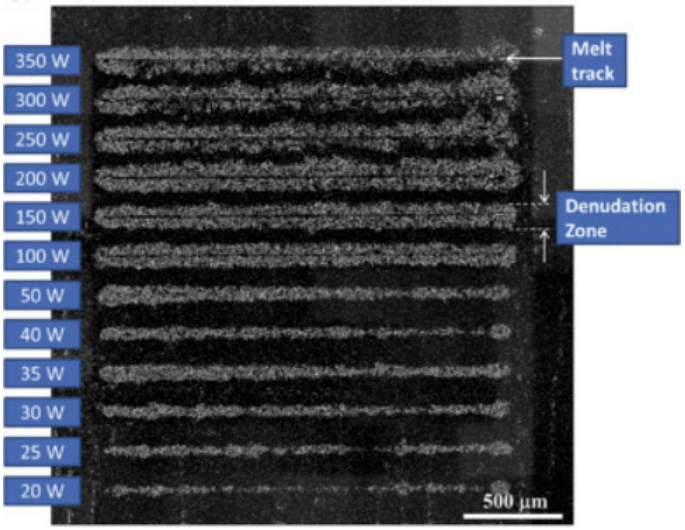

Figure 4. Denudation zone around the melt tracks for various laser power and a constant scan rate of 2 m/s [15].

Vaporization of metallic components of the powder substrate can lead to a loss of alloying elements, reduce part density, and cause microstructural defects. Defects include keyhole/gas porosities, spatter, and cracks. Consequently, the vaporization alters the metallic composition, severely weakening the mechanical properties of the LPBF-printed part, including the ultimate tensile strength, corrosion resistance, and microstructural creep. Vaporization occurs when the intensity of the vapor pressure at the molten melt pool surface is higher than the pressure in the surrounding environment. The surplus pressure difference drives the vapors containing the alloying elements to eject away from the surface [17]. Only certain volatile metals are very susceptible to vaporization at very high temperatures. Metals, including Mg, Zn, and Al, can quickly vaporize due to the elements' low boiling points [18]. Figure 5 shows how metal vaporization can disperse un-melted powder particles during scanning [17].

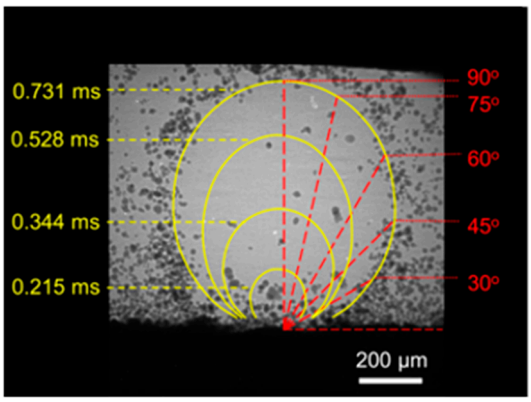

Figure 5. Angular powder velocity tracing path caused by metal vaporization [17].

Environmental effects involve the protective shield of inert gases during the LPBF process. Inert gas conditions play a role in the outcome of surface quality. The three most common shield inert gases used in the LPBF process are argon (Ar), nitrogen (N_2), and helium (He). The type of protective inert gas used during the printing process can affect the part density. One study reported that LPBF-printed SS316L parts under a He environment exhibited a 10% density loss compared to a fully dense part. Under Ar and N_2 environments, the parts had near total density values. The density decrease is due to the He environment restricting the laser interaction and causing some energy loss. An Ar gas supply can overcome the energy losses caused by metal vaporization and ionization processes [19]. Figure 6 compares the melt pool geometry during scanning with inert

(N_2) and air atmosphere, showing a much larger and more chaotic melt pool under an air environment for air compared to inert N_2 gas [19].

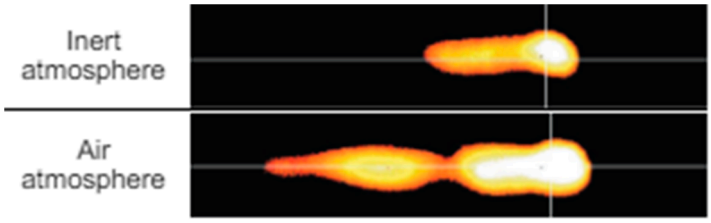

Figure 6. Comparison of melt pool during scanning with inert (N_2) and air atmosphere [19].

2.3. Microstructure Defects

Microstructure defects in LPBF, known as porosities, are voids/gaps that can negatively impact the microstructural integrity and part homogeneity. Heterogenic microstructures often occur through the evolution of the build with each subsequent scan. Porosities can be broken down into three main types, namely: (1) lack of fusion (LOF) porosities, (2) gas porosities, and (3) keyhole porosities. Porosities can form due to powder/elemental impurities. Each porosity type can be attributed to particular sets of process parameters and material properties. Porosities can lead to severe metallurgical defects in lower part density and adversely affect the texture and mechanical performance.

LOF porosities are caused by insufficient laser power and high laser scanning speeds and usually occur at the melt track layer interface. Often associated with the balling effect, the high scan speed and low laser power provide insufficient time for the powder to melt [20]. Poor heat penetration causes the surface of the current layer to become rough and obstructs the molten melt pool flow, causing interlayer defects. Irregular powder particles, such as tiny satellites attached to powder particles, broken powder particles, and dendrite powder particles, have been shown to act as friction points that reduce the powder flowability, allowing for voids to form [21]. Figure 7 highlights LOF porosities in an SS316 LPBF-printed part [22].

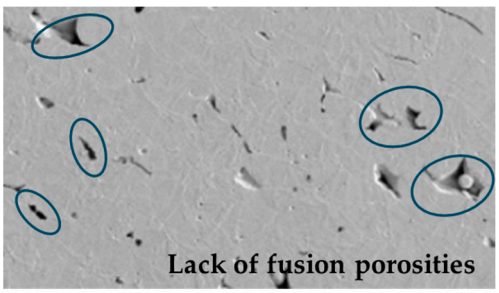

Figure 7. SEM imagery showing various LOF porosities locations (circled) [22].

Gas porosities are typically caused by gas entrapment, the supersaturation of dissolved gases, or chemical reactions. It can also be attributed to process parameters, environmental conditions, and contaminants such as oxides, moisture, and foreign particles. Gas pores form when the equilibrium pressure of the gas overwhelms the combined atmospheric, hydrostatic, and capillary pressures during the LPBF process. Like LOF pores, increasing the laser scan speed while maintaining sufficient laser power allows less time for the powder to melt entirely, providing gas retention opportunities for the solidifying melt pool. Figure 8 highlights the location of gas pores in an SS316 LPBF-printed part [23].

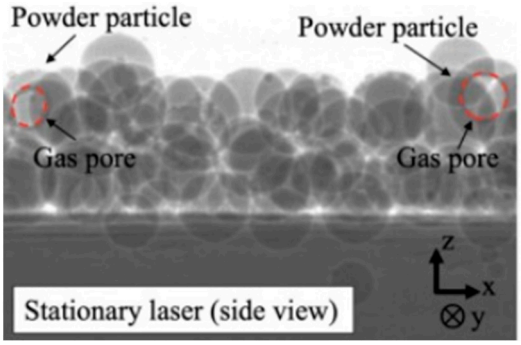

Figure 8. X-ray radiographic images highlighting gas pore's locations [23].

Keyhole porosities are also known as depression defects and typically occur when the laser power density is excessively high. The high laser power causes deeper melting pools to form, and the overheating causes the low melting point elements within the alloy to vaporize in the form of gas bubbles.

The vaporization leads to the instability of the melt pool and creates a recoil pressure inside the melt pool that can push away the melted liquid [24]. As the depressed melt zone rapidly solidifies, the gases are trapped, causing the formation of spherical pores. Figure 9 highlights a keyhole pore in an SS316L LPBF-printed part [25].

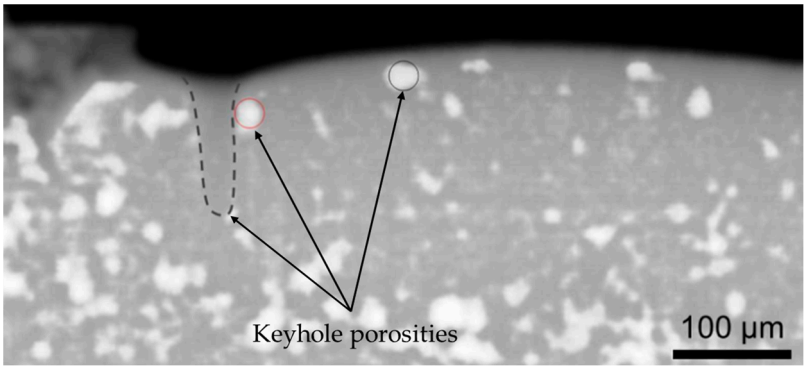

Figure 9. X-ray imaging highlighting the location and shape of keyhole pores [25].

Impurities in the powder substrate can have a positive and/or negative influence on the mechanical behavior of the LPBF-printed part. Impurities have been known to enhance mechanical behavior, strength, and ductility but can also lead to lower corrosion resistance. The impurities most commonly associated with the LPBF process include carbon, oxygen, nitrogen, hydrogen, and chlorine [26]. Oxygen is the most common impurity and can cause oxides to form. Lower energy impurities lead to smaller grains, more grain boundaries, increased nucleation, and diminished corrosion resistance [27].

2.4. Mechanical Defects

Thermal stresses induce mechanical defects; mechanical stresses are induced by temperature gradients in a material. In LPBF, the part undergoes thermal stresses during scanning or shortly after several subsequent scans, producing a large temperature gradient. The high thermal energy gradient induced by the laser beam causes the top layers of the solid to expand and induce elastic compressive stresses thermally. Once the yield stress point is exceeded, plastic deformation of the top layers occurs. As the plastically deformed layers rapidly cool down, the printed material layers contract and bend oppositely. It converts the compressive stresses into residual tensile stresses that can induce cracking. Shortly after scanning, the tensioned layer cools, which causes the layer to shrink faster due to the slight differences in thermal conductivity, causing a thermal contraction by the lower, colder layers. Due to the solid metallurgical connection of both layers, contraction is

inhibited, causing tensile stresses to the upper and compressive stresses in the lower layers, as shown in Figure 10 [28]. In extreme cases, high thermal stress can cause part distortion, shrinkage, cracking, warping, and delamination.

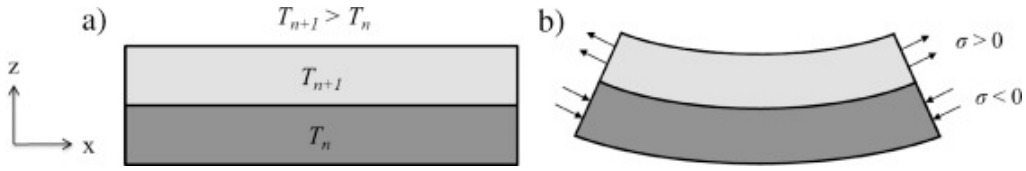

Figure 10. Unique residual stress distribution (compression and tension) seen in AM, showing the cool-down phase inducing residual stress developed at the solid layer connection during (**a**) heating and (**b**) cooling [28].

Liquation cracking mainly depends on the stability of the liquid film of the melt pool and local stress concentration [29]. High laser energy and lower powder thermal conductivity contribute to liquid film instability and rapid thermal cycling. Thermal cycling induces tensile stress and causes cracking. Introducing some alloying element that can limit the solidification temperature would alter the chemical composition of the molten pool to prevent cracking [30]. Figure 11a,b shows the geometry of liquation cracks in an IN718 LPBF-printed part [31].

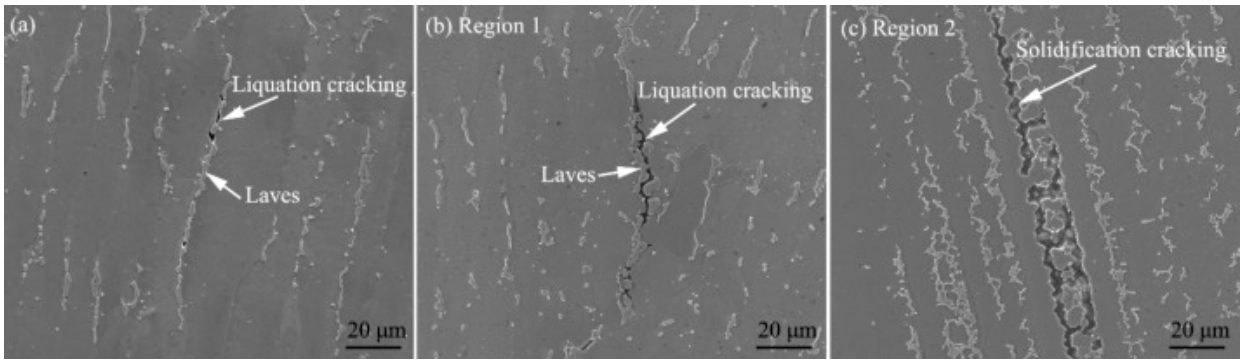

Figure 11. Comparison of liquation (**a**,**b**) and solidification (**c**) cracking in an IN718 LPBF-printed part [31].

Solidification cracking is also known as cold cracking, a type of crack that occurs in the latter stages of the solidification process. Near the end of solidification, dendrites have almost fully grown into equiaxed grains. These dendrites are separated by a slight residual liquid strip [32]. Insufficient convection in the diminishing liquid region causes weak spots to form and causes the formation of micro-cracks that can propagate and be enlarged. Alloys with a wide solidification temperature range are more susceptible to solidification cracking than alloys that solidify over a narrow temperature range due to the accumulated thermal strain proportional to the temperature range [27]. Solidification cracks can be eliminated by adopting a re-melting strategy or post-build machining. A sure way to reduce solidification cracking is to avoid rapid cooling. Figure 11c shows the geometry of solidification cracks in an IN718 LPBF-printed part [31].

Delamination is a unique cracking behavior observed in AM LPBF builds. Delamination is caused by macroscopic residual stresses originating from spatial thermal gradients [33]. The uneven expansion and shrinkage of the part during thermal cycles results in non-uniform inelastic strain and, hence, delamination [34]. Delamination appears as cracking between deposition layers, often resulting in complete part failure. Figure 12 highlights delamination cracking in an SS304L LPBF-printed part [35].

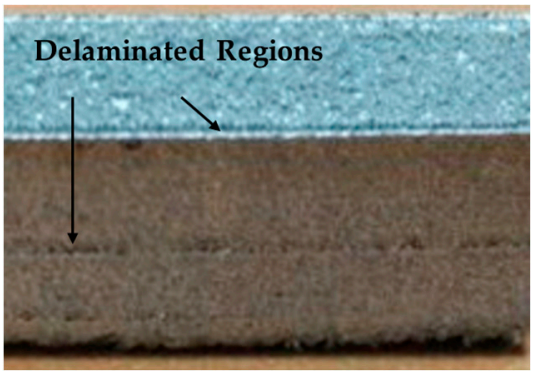

Figure 12. Delamination cracking within an SS304L LPBF-printed part [35].

3. LPBF Sensing Techniques

The LPBF part quality and existing defects can be characterized using unique sensing techniques. These techniques can be divided into: (1) optical, (2) thermal, (3) acoustic, (4) ultrasonic, and (5) miscellaneous techniques (Figure 8). Combinations of these techniques are employed to provide further insight into the investigated phenomena. In this section, the associated technologies associated with each technique are described. Research efforts conducted using these technologies to assess part quality and defect detection are provided. The advantages and disadvantages of each technology are mentioned. A description of each technology's defect detection capabilities is included in Figure 13.

Sensing Techniques Applicable for LPBF Defect Detection

1. Optical

Electron

- Scanning Electron Microscope (SEM)
- Transmission Electron Microscope (TEM)
- Electron Backscatter Diffraction (EBSD)
- Energy-Dispersive X-ray Spectroscopy (EDS)
- X-Ray Photoelectron Spectroscopy (XPS)
- Electron Probe Micro-Analyzer (EPMA)

X-Ray

- X-ray Computed Tomography (XCT)
- X-Ray Diffraction (XRD)

Visible Light

- Optical Microscope (OM)
- Confocal Laser Scanning Microscopy (CLSM)
- Digital Single-Lens Reflect (DSLR)
- Digital Image Correlation (DIC)

Others

- Optical Emission Spectroscopy (OES)
- Atom Probe Tomography (APT)

2. Thermal

- Thermal Imaging Cameras (TIC)
- Infrared Thermography Cameras (IRTC)
- Short-Wave Infrared Imaging (SWIR)
- Single-camera Two-wavelength Imaging Pyrometry (STWIP)
- Infrared Pyrometer Sensors (IPS)
- Differential Scanning Calorimeters (DSC)

3. Acoustic

- Acoustic Emission Spectroscopy (AES)
- Fiber Bragg Grating (FBG)
- Nonlinear Reverberation Spectroscopy (NRS)

4. Ultrasonic

- Immersion Ultrasonic (IU)
- Laser Ultrasonic (LU)
- Pulsing Ultrasonic (PU)
- Resonant Ultrasound Spectroscopy (RUS)
- Phased Array Ultrasonic Testing (PAUT)

5. Miscellaneous

- Eddy Current Testing (ECT)
- Atomic Force Microscopy (AFM)
- Gas Pycnometers (GP)
- Conversion Electron Mössbauer Spectroscopy (CEMS)
- Neutron Diffraction (ND)
- Electrochemical Impedance Spectroscopy (EIS)

Figure 13. Sensing techniques for LPBF part defect detection.

3.1. Optical Techniques

Optical techniques are the most commonly employed in assessing part quality and detecting LPBF defects. Optical techniques can probe the sample's external surface and internal structures using electron trajectories or specific electromagnetic radiation ranges.

Sources that produce valuable and traceable optical behaviors in the specimen include electron beams, X-rays, lasers, electric sparks, and light. This subsection is divided into four categories: optical techniques using an electron source, an X-ray source, a visible light source, and optical techniques using other sources. Tables 1–5 detail literature sources displaying combinations of optical sensing techniques to quantify LPBF defects. In each table, checkmarks are made to represent the following technologies used to detect defects for the shown references.

3.1.1. Techniques with Electron Source

Scanning electron microscopy (SEM) uses a focused beam of electrons to analyze the specimen's surface topography and material composition. The focused electron beam passes through scanning coils in the electron column that deflect the beam so the object can be scanned. Once the electron beams interact, random scattering and absorption cause the electrons to lose energy. High-energy electrons are reflected by elastic scattering, secondary emission by inelastic scattering, and electromagnetic radiation emission. The scattered electrons are captured using detectors, and the electron signals are converted to voltage signals using photomultipliers. Collecting the measured intensity of the detected signal and the electron beam's recorded position enables the construction of a 2D image of the part. SEM technologies are frequently equipped with multiple detectors to detect specific emissions. Electron backscatter diffraction (EBSD) and energy-dispersive X-ray spectroscopy (EDS) are often paired with SEM technology to provide further information on the specimen. The advantages of using SEM include its high versatility, high image resolution, easy operation, fast scanning rate, and non-destructive nature. The disadvantages of SEM include its large size, high price, vacuum environment requirements, minor radiation exposure risk, long sample prep time, and sensitivity to interferences (electrical, magnetic, and vibrational). An example of SEM imagery of an LPBF-printed part highlighting un-melted spherical powder is provided in Figure 14 [36].

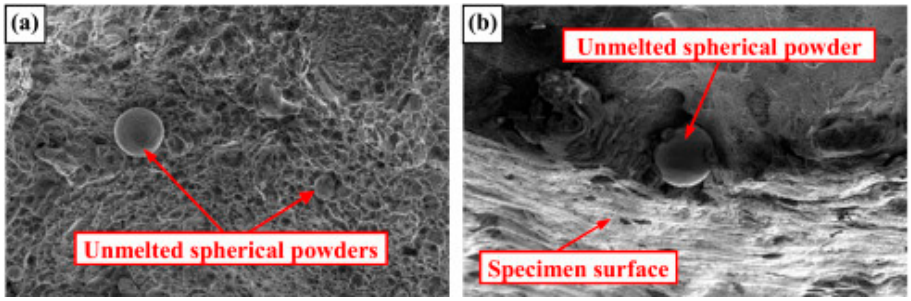

Figure 14. Example of SEM imagery provided by [36], highlighting un-melted spherical Ti6Al4V powders (**a**) inside of the LPBF specimen post-build and (**b**) on the free surface of the specimen.

Transmission electron microscopy (TEM) is comparable to the SEM in that a focused beam of electrons is directed toward the sample. However, in TEMs, the sample is located in the middle of the column. The transmitted electrons passing through the sample before they are collected provide the sample's internal structure, including crystalline structure, morphology, and stress state information. Once the transmitted electrons pass through the sample, they travel through a series of intermediate and projector lenses below the sample and directly produce an image on a fluorescent screen or charge-coupled device (CCD) camera. Unlike SEMs, which only produce 2D surface topographical imagery, TEMs can also produce 2D images of internal structures. SEMs have a much larger maximum field of view (FOV) than TEMs, though the magnification capabilities of TEMs are much higher than those of SEMs. EDS has often been coupled with TEM to produce elemental and atomic-bonding information. TEMs have been widely used to analyze interfacial grain boundaries, dislocation networks and densities, and particle precipitation. The advantages of using TEM are practically the same as those of SEM. The disadvantages of using TEM

are also the same as those of SEM, with the added negative of TEM being destructive to the sample. An example of TEM imagery is provided in Figure 15, showing the location of stacking faults in an LPBF-printed austenitic stainless-steel sample [37].

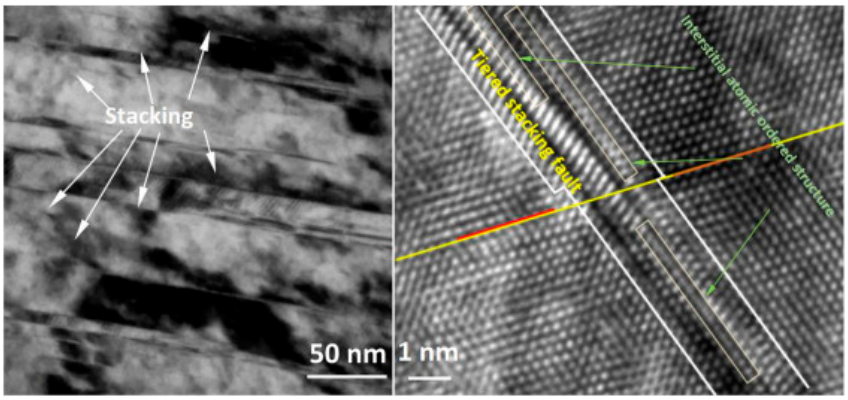

Figure 15. Example of TEM imagery provided by [37], showing locations of stacking faults and interstitial atomic ordered structures of an LPBF supersaturated austenitic stainless-steel-printed part.

Electron backscatter diffraction (EBSD) detector is an SEM-compatible technique where the electron beam is scanned across the surface of a tilted crystalline sample. The electronic source is provided by a field emission gun rather than a thermionic emission mechanism. A similar technology often associated with EBSD is electron channeling contrast imaging (ECCI). ECCI is geared explicitly towards imaging and characterizing lattice defects, while EBSD is geared towards more detailed crystallographic analysis. ECCI has been used in LPBF printing analysis to visualize precipitates in the printing process due to the non-equilibrium between the melting and solidification processes [38,39]. In EBSD, the diffracted electrons at each point form a pattern that can be detected using a backscatter detector (BSD) that produces kernel average misorientation (KAM), pole figures (PF), and inverse pole figure (IPF) maps [40].

KAM maps display the average misorientation between each pixel concerning its surrounding pixels [41]. It enables semi-quantitative analysis of strain distributions at near-surface depths in deformed microstructures. PFs and IPFs are stereographic projections where the orientations are plotted relative to the sample and crystal axes [42]. Often, PFs provide texture, and IPFs are used as a color key for crystal orientation maps (COMs). The advantages of EBSD include its relatively fast detection and analysis rate, its ability to scan and map large sample areas (mm) of interest, and its non-destructive nature.

Additionally, it determines grain boundaries without etching and evaluates crystallographic textures. The disadvantages of EBSD include its need for vacuum compatibility and potential extensiveness. It requires precise surface preparation, including polishing, and multiple attempts using the EBSD to achieve high-quality results. Figure 16 displays an example of EBSD IPF imagery, highlighting changes in crystallographic texturing indicating grain boundaries and potential defects [43].

Energy-dispersive X-ray spectroscopy (EDS, EDX) is a surface analytical technique that measures the electronic structure behavior of the material when exposed to an electron beam. The exposure of an electron beam causes an electron in the inner shell of the material to be ejected, forming a vacant inner shell electron position. The produced X-rays from the ejection can be accumulated at all produced wavelengths from the sample using a solid-state semiconductor detector.

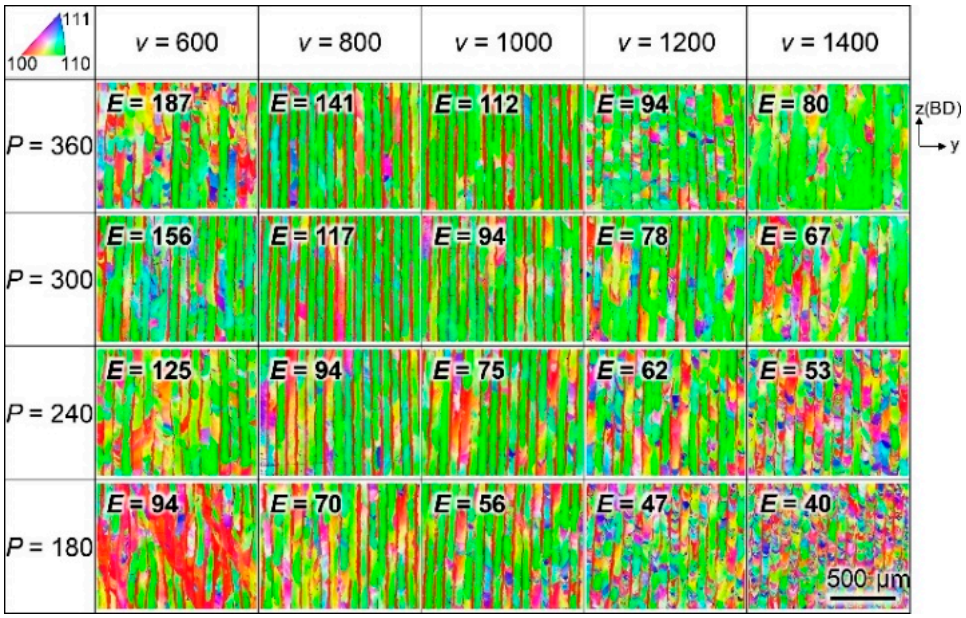

Figure 16. Examples of EBSD IPF imagery provided by [43] showing the change in crystallographic texturing along the build direction for various LPBF power (P) scan speeds (V).

EDS is used to determine and quantify the material's elemental composition. The advantages of EDS include its short measurement time, no need for pre-treatment processes such as surface polishing, and compact size. The disadvantages of EDS are that it could potentially provide poor energy peak resolution due to bremsstrahlung background interference and is somewhat inaccurate for heterogenous materials. An example of how EDX is utilized in defect detection is provided in Figure 17, showing how EDX can be used in tandem with SEM to analyze defects [44].

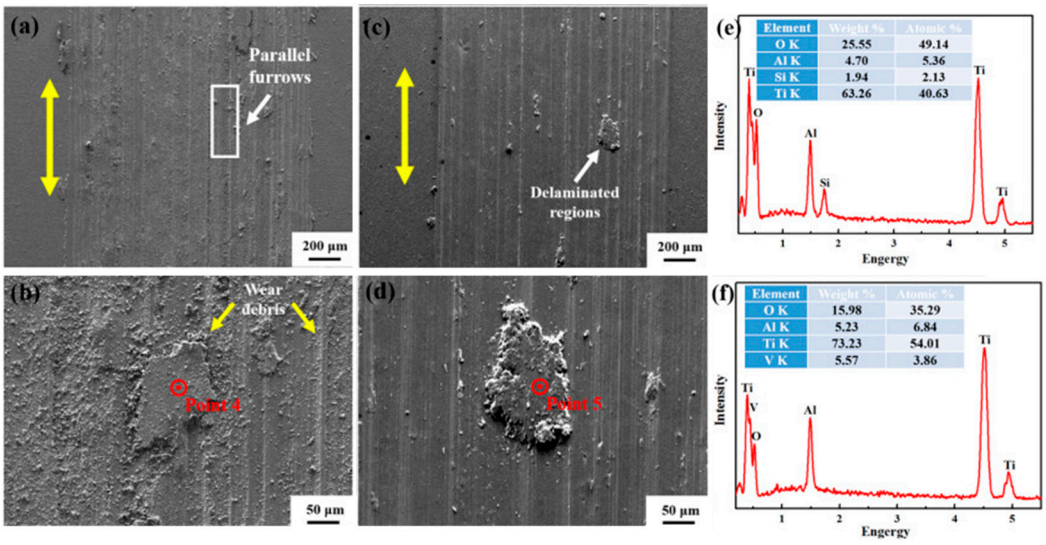

Figure 17. An example provided by [44] of EDX spectral data cross-analyzed with SEM micrographs, showing the worn surfaces after friction testing of an LPBF-printed part (large arrows indicate scan direction). (**a**,**b**) 0 wt% TiB2 sample showing parallel furrows and wear debris; (**c**,**d**) 3 wt% TiB2 sample showing a delaminated region defect; (**e**,**f**) corresponding EDX analysis results for point 4 (**b**) and point 5 (**d**).

X-ray photoelectron spectroscopy (XPS) devices use the photoelectric effect like EDS to generate signature signals produced by the photoelectrons akin to a specific element.

Unlike EDS, which is typically coupled with SEMs or TEMs, the XPS analyzer is a separate device that explicitly uses the detection data of the ejected electrons to determine the near-surface regional chemical composition. The advantages of XPS are that it collects data quickly, is efficient in detecting surface contaminants, and is non-destructive to the sample. The disadvantages of XPS are that significant relative errors are common and that the reproducibility of the same data at different facilities is unsteady. Figure 18 shows an example of XPS data for an LPBF-printed part [45].

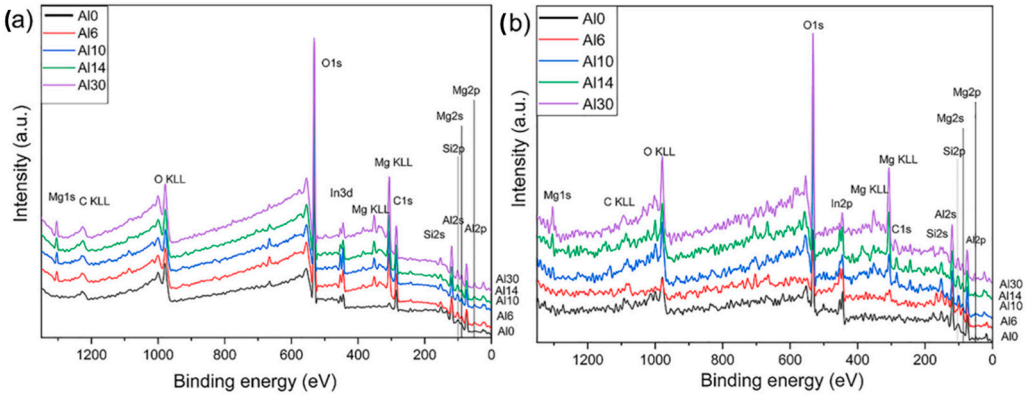

Figure 18. Example of XPS survey spectra provided by [45] for an AlSi10Mg LPBF-printed part at (**a**) the free surface and (**b**) an etch depth of 4 nm.

Electron probe micro-analyzer (EPMA) works like SEMs, bombarding parts with an electron beam and emitting X-rays at wavelengths characteristic of the analyzed elements. However, EPMAs are equipped with various crystal spectrometers that enable quantitative chemical analysis at high sensitivity. The advantages of EPMA analysis are that it is considered superior to EDS analysis and is non-destructive to the sample. The disadvantages of EPMA include complex sample preparation into polished and flat sections, overlapping peak positions hinting at inaccurate readings, and the inability of various valence states to differentiate. Figure 19 shows how EPMA can be used to analyze LPBF micro-cracking [46].

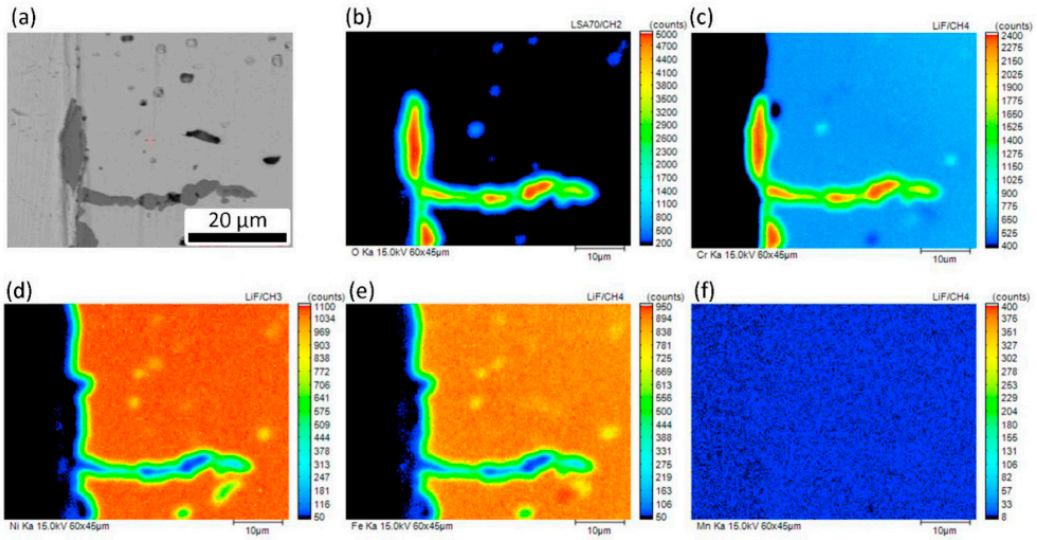

Figure 19. Example of EPMA imagery provided by [46], highlighting a micro-crack observed in a cross-section of a GH3536 superalloy LPBF-printed part along with element distribution of the scale.

Table 1. Combinations of optical techniques using an electron source for various customized or less investigated LPBF-printing powder materials.

Material	SEM	TEM	EBSD	EDS	XPS	EPMA
Stainless-Steel-Based Alloys						
SS316L [41,47]			✓			
GH3536 [46]	✓	✓		✓		✓
Custom austenitic SS. [37]	✓	✓				✓
SS316L [48–51], 1.2767L tool steel [52]	✓					
SS316L [53,54], Maraging steel, 2205 Duplex SS. [55,56]	✓	✓	✓	✓		
17-4PH SS [57]		✓		✓	✓	
Maraging steel [58]	✓	✓	✓	✓		
AISI 420 Steel [59]	✓			✓		
Titanium-Based Alloys						
Ti6Al4V [43], IN718 [60]	✓	✓		✓		
TiB/Ti6Al4V [44]	✓	✓		✓	✓	
TiNi [61], NiTi [62]	✓	✓	✓	✓	✓	✓
Ti6Al4V [63], Ti and Ti-13Nb-13Zr [63], Ti–43Al–9V-0.5Y [64]	✓	✓	✓			
Nickel-Based Alloys						
IN625 [65]	✓		✓	✓	✓	
Hastelloy X [66]	✓			✓		
Ni + SAF2205-22Cr [67], IN718 [68,69]	✓		✓	✓		
Nickel-based alloy [38], IN718 [70,71]	✓		✓			
IN718 [60], alloy 247LC [72]	✓	✓		✓		
Aluminum-Based Alloys						
AlSi7Mg0.3 [73], AlSi10Mg [72–74], Al-33Cu [75]	✓					
Al2024 [74]	✓		✓	✓		
AlSi10Mg [76,77]	✓			✓		
AlSi10Mg [78,79]	✓		✓			
Al-3.6Zn-0.6Mg [79]	✓	✓	✓	✓		✓
AddalloyTM [80], AlSi10Mg [81]	✓	✓	✓	✓		
Other alloys/elements						
Ta [82]	✓			✓	✓	
Zn alloy [83]	✓			✓		
Nb [84]	✓		✓			
Ag [85], W [86]	✓					

3.1.2. Techniques Using an X-ray Source

X-ray computed tomography (XCT) devices utilize an X-ray source to produce 2D radiographic slice imagery of the investigated object from many directions. Using the stack of cross-sectional 2D radiograph slices, a reconstruction algorithm is employed to

generate a compiled 3D morphology image of the object [87]. The advantages of XCT are that it requires little or no sample preparation and is non-destructive to the sample. The disadvantages of XCT are that it is very time-consuming and expensive, and it can produce blurred material boundary images. An example of XCT analysis of LPBF-printed part porosities is provided in Figure 20 [88].

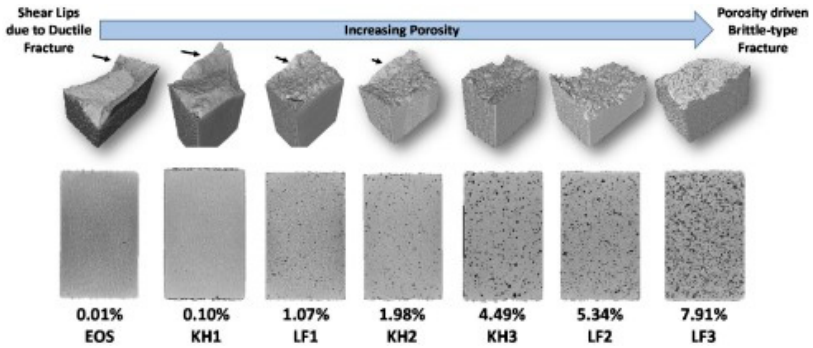

Figure 20. Example of XCT cross-sections of coupon samples with various porosities provided by [88]. The increase in brittle fracture is attributed to the porosity regardless of defect type.

X-ray diffraction (XRD) machines bombard incident X-ray beams at the investigated crystalline sample to analyze the crystallographic condition. The sample's crystalline structure causes the X-rays to diffract in many specific directions. Information on the angles and intensities can be used to determine the 3D electron density distribution. This distribution can estimate the average position of the atoms in the crystal and provide knowledge regarding the presence of defects within the crystal. The advantages of XRD are that it is a non-destructive technique, requires little to no sample prep time, and does not need vacuum operating conditions. The disadvantage of XRD is that it is considered less accurate for small crystalline structures and can produce peak overlays when performing non-isometric crystalline structure pattern indexing. Figure 21 shows an example of XRD pattern results for LPBF SS316 powder [89].

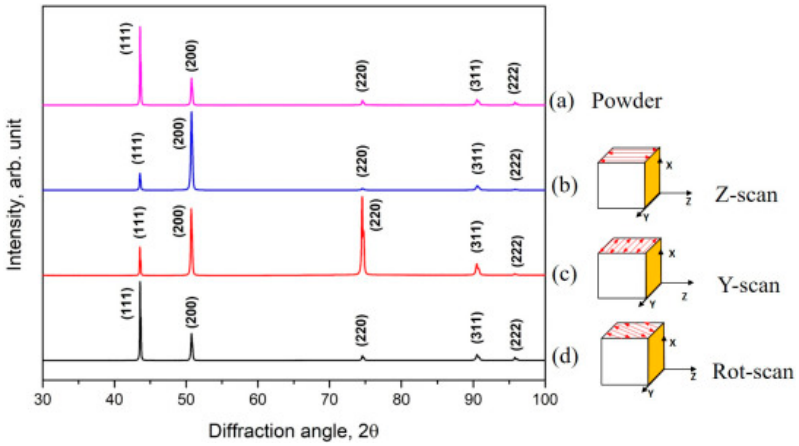

Figure 21. Example of XRD pattern results provided by [89], showing results for (**a**) the powder and (**b**) Z-scan direction, (**c**) Y-scan direction, and (**d**) 67° rotation scanning direction.

3.1.3. Techniques Using a Visible Light Source

Optical microscopy (OM, OT) utilizes visible light in combination with a system of lenses to produce magnified images of the sample. OM is called a transmission light microscope (TLM) or light microscope. The advantages of OM are that it is typically easy to use, small and lightweight, unaffected by electromagnetic fields, requires no radiation, and requires little training and maintenance. The disadvantages of OM are that it cannot

magnify to their level and produces lower-resolution pictures. Figure 22 displays an example of optical microscopy images of various defects in an LPBF SS316L [90].

Confocal laser scanning microscopy (CLSM) uses laser light to scan the sample using different patterns and generate imagery. The laser penetrates the sample deeper than light from a standard lightbulb, allowing for 3D imagery of controlled depth. The advantages of CLSM are that it can provide high spatial-resolution imagery with reduced background noise and good accuracy. The disadvantages of CLSM are that it is more expensive than light microscopes, has limited penetration depth capability, and has a time-consuming sample preparation procedure. An example of CLSM showing high surface roughness in a Ti6Al4V LPBF-printed part is provided in Figure 23 [91].

Table 2. Combinations of optical techniques using an X-ray source for various customized or less investigated LPBF-printing powder materials.

Material	XCT	XRD
Stainless-Steel-Based Alloys		
1.2767L Tool Steel [52], SS316L [47,92], RAFM steel [93], 18Ni maraging steel [94]	✓	✓
Custom austenitic SS. [36], SS316L [90,95], AISI 420 Steel [59,96]		✓
A800H [97], SS316L [98–100]	✓	
Titanium-Based Alloys		
Ti-TiB [101,102], Ti6Al4V [88,103,104], Ti64 [105]	✓	
TiNi [61], Ti6Al4V [91,103], Ti–43Al–9V-0.5Y [64], Ti6Al7Nb [106]		✓
NiTi [62], Ti6Al4V [107,108]	✓	✓
Nickel-Based Alloys		
IN625 [109], IN718 [69,110,111], Ni10Cr6W1Fe9Ti1 [112]		✓
Hastelloy X [66], nickel-based superalloy [113]	✓	
IN718 [114]	✓	✓
Aluminum-Based Alloys		
AlMgScZr [115], AlSi10Mg [116,117]	✓	✓
Al-33Cu [75], AlSi10Mg [77]		✓
AlSi10Mg [118–120]	✓	
Other alloys/elements		
Ta [82], CoCrMo [121], Nb [84], Cu10Zn [122]		✓
Zn-alloy [83], Ag [85], CoCr [123]	✓	

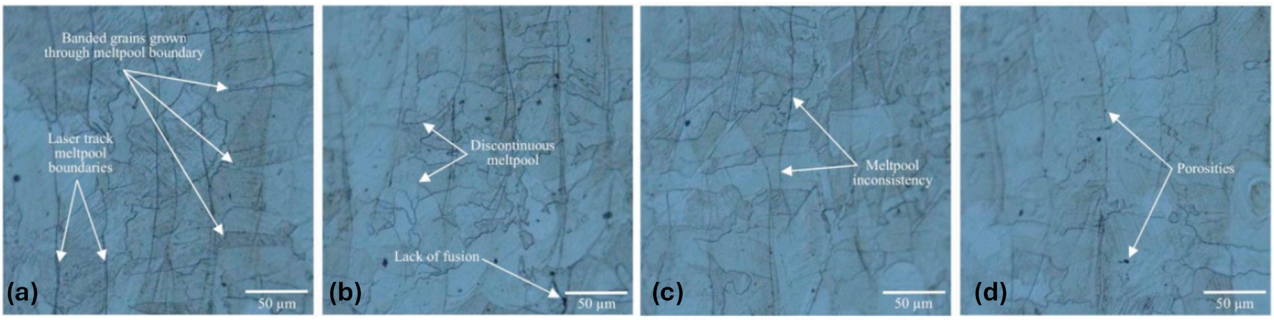

Figure 22. Example of OM imagery provided by [90] showing several types of microstructural defects at the (**a**) front, (**b**) argon outlet, (**c**) back, and (**d**) argon inlet locations of an SS316L part.

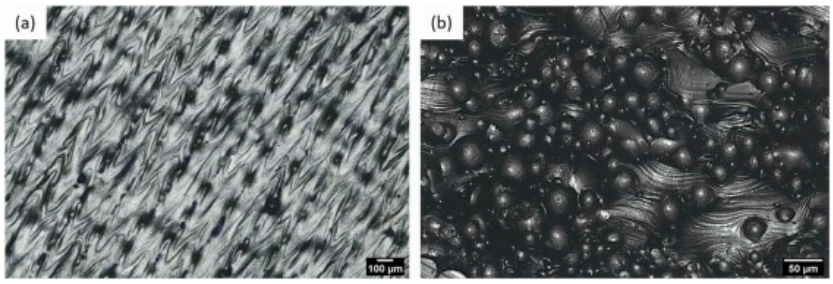

Figure 23. Example of CLSM images provided by [91] showing the high surface roughness of a Ti6Al4V LPBF-printed surface on the (**a**) XY-plane and (**b**) XZ-plane. CLSM can measure the height of surfaces, pinpointing potential surface defects [124].

Digital single-lens reflect (DSLR) cameras combine optics and the single-lens reflex camera mechanism with an image sensor to record the images. A DSLR uses the reflex scheme, where light travels through several lenses and is then reflected by a mirror that sends the image through a camera prism. The reflex design scheme is the main difference between a DSLR and other digital cameras. The advantages of DSLR cameras are that they are widely available and provide better image quality than other cameras. The disadvantage of DSLR cameras is that they are relatively expensive. A comparison of the CAD model and DSLR imagery of an SS316L LPBF-printed part is provided in Figure 24 [125].

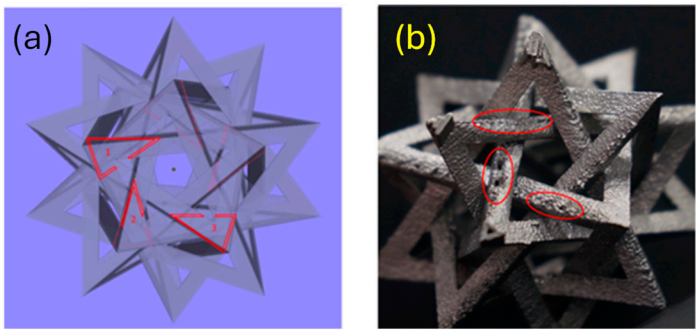

Figure 24. Comparison of (**a**) CAD model and (**b**) DSLR imagery of an SS316L LPBF-printed part provided by [125], highlighting locations of intentionally designed defects.

Digital image correlation (DIC) is a technique that records 2D strain and deformation changes on the surface of the investigated specimen. DIC is an optical technique combining image registration and tracking methods to measure changes in 2D images [126] accurately. DIC is accomplished using two charge-coupled device camera measurements, identifying 3D surface contour and surface strain distributions by measuring displacement in the depth direction. Via digital camera imagery, the surface characteristics can be allocated to image pixels, and the comparison between the current digital image and the next one can be used to calculate the deformation of the object [127]. The advantage of DIC is that it can provide high-precision strain measurements. The disadvantage of DIC is that it cannot account for rigid-body rotation.

3.1.4. Techniques Using Other Sources

Optical emission spectroscopy (OES) uses an excitation mechanism like an electric spark or arc source to produce a high-voltage pulse between the tip of a counter-electrode and the sample surface. This high voltage pulse ionizes the atmospheric gap, causing it to become conductive with low impedance and generating a stable current and plasma. When electrical discharge interacts with an atom, electrons in the atom's outer shells are ejected, creating a vacancy. Higher-orbit electrons will drop down to fill the vacancy, emitting excess energy as the electron moves between the two energy levels. Electron transport causes element-specific light, known as optical emission. The characteristic light can be

processed to generate a spectrum showing the light intensity peaks compared to their wavelengths. These peak wavelengths can then be used to identify the element. The advantages of OES include very high accuracy and precision. The disadvantage of OES is the possibility of spectral interference affecting chemical composition percentages. Table 5 displays OES data showing the chemical composition of various steel-based LPBF-printed cubic samples [128].

Atom probe tomography (APT) device provides 3D compositional mapping of materials by holding the specimen in front of a counter electrode located a set distance away and connecting it to a direct current high-voltage power supply. The pulsing high voltage causes field evaporation, followed by a measurable flight time of each ion. The time of flight is measured using a single-particle delay-line detector that converts the impact of a single ion into hundreds of thousands of electrons. The electrons are collected, and the impact position is calculated using the processed electronic signals detected at each end of each delay line. The advantages of APT are its atomic resolution capability and ability to identify chemical compositions in 3D space. The disadvantages of APT are that it is destructive to the sample, is chemically sensitive compared to other technologies, and only analyzes tiny sample sizes. Figure 25 shows APT analysis for an LPBF 2205 duplex stainless-steel-printed part, showing a 3D map of the different elements in the sample [56]. Table 5 below summarizes all-optical techniques that use other sources.

Table 3. Combinations of optical techniques using a visible light source for various customized or less investigated LPBF-printing powder materials.

Material	OM	CLSM	DSLR	DIC
Stainless-Steel-Based Alloys				
SS316L [41,42,53,92,128], 17-4PH SS. [129], A800H [130], RAFM steel [93], CLF-1 steel [131], 17-4 PH SS [13], SS316L-SS431 [132], AISI 420 Steel [59,96]	✓			
GP-1 Steel [133], SS316L [134–136]			✓	✓
SS316L [40,51,124]		✓		
Titanium-Based Alloys				
Ti6Al4V [137–139], TiB [140], Ti [141], NiTi [62], TiB2-B4C [142], Ti6Al7Nb [106]	✓			
TiNi [61]		✓		
Ti–43Al–9V-0.5Y [64]			✓	
Ti6Al4V [91,143]	✓	✓		
Nickel-Based Alloys				
Haynes 282 [144], Ni10Cr6W1Fe9Ti1 [112], Nickel-based superalloy [113]	✓			
IN718 [111,114]				✓
IN718 [110]	✓		✓	
Aluminum-Based Alloys				
AlMgScZr [115]		✓		✓
AlSi10Mg [8,77,81,102], AlSi7Mg0.3 [73], Al2024 [74]	✓	✓		
Other alloys/elements				
Ta [82], Nb [84], Ag [85], Cu [145], CoCrMo [121], Cu10Zn [122]	✓	✓		

Table 4. Combinations of optical techniques using other sources for investigating LPBF-printed parts.

Material	OES	AFM
SS316L [128]	✓	
SS316L [95,146]		✓
IN718 [147]		✓
IN718 [148]	✓	
Ta [82]		✓

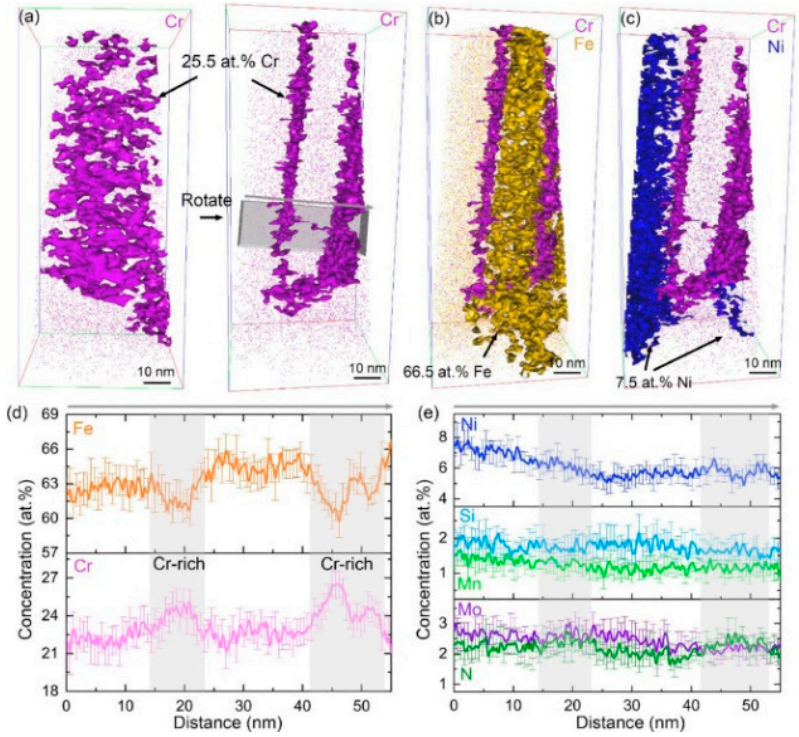

Figure 25. Example provided by [56] showing the APT analysis results for the austenitic phase of a 2205 duplex stainless-steel LPBF-printed part. (**a**) Atom maps of Cr species viewed at two different angles, (**b**) overlayed atom map of Cr and Fe species, (**c**) overlayed atom map of Cr and Ni species, (**d**) 1D concentration profiles of Fe and Cr, (**e**) 1D concentration profiles of Ni, Si, Mn, Mo, and N.

Table 5. Example of OES data provided by [128] showing the chemical compositions of various steel-based LPBF-printed cubic samples.

Name	Processed	C	Si	Mn	Cr	Mo	N	Ni	Fe	PREN
AISI 316L	Cast/Rolled	0.022	0.32	1.67	16.6	2.02	0.08	10.02	Bal.	25
AISI 316L	LPBF	0.022	0.64	1.39	16.6	2.14	0.06	10.54	Bal.	25
M7-3	LPBF	0.029	0.61	1.08	18.9	2.63	0.09	9.02	Bal.	30
M5-5	LPBF	0.030	0.61	1.11	20.4	2.76	0.14	7.31	Bal.	32
M3-7	LPBF	0.026	0.67	1.04	21.1	2.98	0.15	6.73	Bal.	33
AISI 318LN	LPBF + SA	0.022	0.70	0.81	22.9	3.23	0.17	5.66	Bal.	35
AISI 318LN	Cast/SA	0.038	0.68	1.27	22.5	3.01	0.17	6.32	Bal.	36
AISI 316L	Cast/ Rolled	0.022	0.32	1.67	16.6	2.02	0.08	10.02	Bal.	25
AISI 316L	LPBF	0.022	0.64	1.39	16.6	2.14	0.06	10.54	Bal.	25
M7-3	LPBF	0.029	0.61	1.08	18.9	2.63	0.09	9.02	Bal.	30

3.2. Thermal Techniques

Thermal techniques utilize differences in temperature and light to assess part quality and detect defects. Thermal techniques can be implemented in situ to monitor the melt pool behavior in LPBF printing. Infrared and thermal imaging cameras (1400–3000 nm and 3000–15,000 nm wavelength range) and pyrometers are used. After solidifying the melt pool, they provide indicative information regarding the specific defects' location, type, and size. Other observed techniques, such as differential scanning calorimeters (DSC), can monitor the changes in heat flow during metal alloys' heating or cooling processes. The heat flow enables tracking temperatures associated with phase transitions to point out potential defect formations.

Thermal imaging cameras (TIC) provide data on temperature variations concerning the subject's absolute temperature and surroundings. Typically, filters are applied to two high-speed cameras that capture two wavelength intensities in thermal imaging. The intensity ratio between the two images can be correlated to temperature values. TIC enabled the analysis of the melt pool dynamics, tracking ejected particles from the LPBF printing process, as shown in Figure 26 [149].

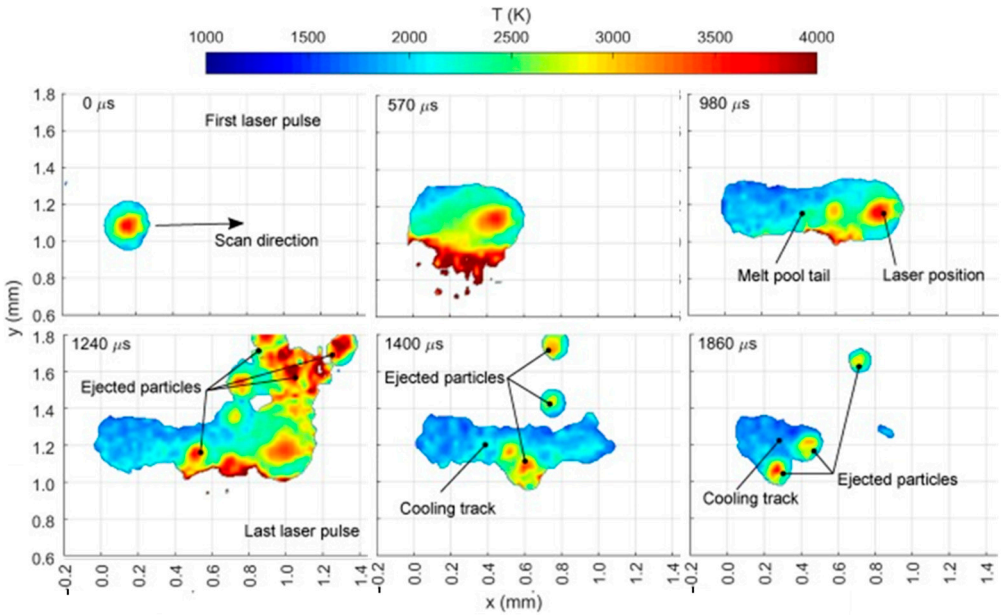

Figure 26. The surface temperature development during the LPBF scanning of an overhanging feature using TIC. Thermal imaging shows ejection particle ejection that can help indicate the location of potential defects [149].

Infrared thermography cameras (IRTC) capture images by detecting short IR energy wavelengths emitted by an object and converting them to temperature values. Defects are detected by locating disturbances in the temperature profile. Santospirito et al. [150] utilized an IR camera to detect defects in LPBF components. A similar study monitored the melt pool characteristics of Ti6Al4V, AlSi10Mg, and NiTinol LPBF-printed parts using a high-speed NIR thermal CMOS camera [151]. Observations made using the NIR camera were compared with XCT measurements of the cut samples, indicating excellent compatibility between the actual defects and what was observed from in situ quality control. A forward-looking infrared (FLIR) camera was used to capture temperature measurements of the molten pool surface of SS316L [152]. Unstable melt track characteristics were observed using the IR camera, which showed spherical formations akin to balling. The evolution of the generated thermal footprint during the LPBF printing process using an IR camera to detect artificially created laser defects was evaluated [153]. The IRTC detected the typical micrometric defects inside the AM part. Artificially created micro-drilled defects in titanium alloy LPBF-printed acetabular cup prostheses using an FLIR camera were captured in a

study by Montinaro et al. [154]. Subsurface defects were detected up to a depth of 1.3 mm in the part. The IRTC captured plume and spatter signatures using near-infrared (NIR) imagery. The intensity and dynamic nature of the plume and spatter during the LPBF printing process were caused by the melting instabilities, including defects such as lack of fusion, cracks, warps, or delamination, which were successfully captured [154]. A method for reliable characterization of the calorimetric signature of fatigue damage was developed using IRTC [25]. Figure 27 shows IR camera images capturing the location of defects and damage to the LPBF-printed part [155].

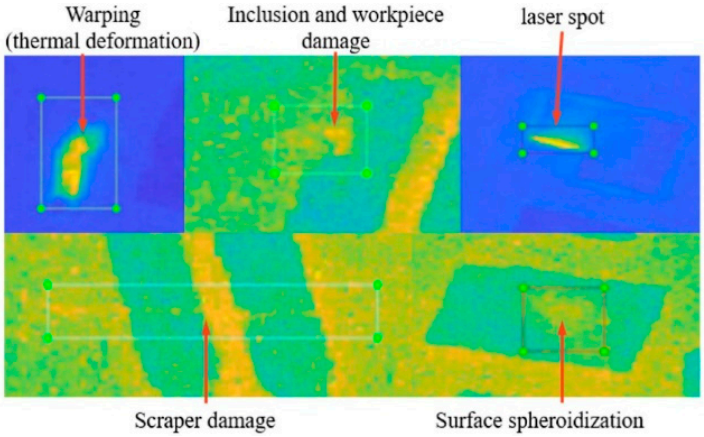

Figure 27. IR camera imaging highlights the location and shape of various defects [155].

Short-wave infrared imaging (SWIR) cameras capture wavelengths between 900 and 2500 nm. The SWIR cameras are superior to alternative thermal cameras for capturing fast dynamic events at high temperatures, such as melt pool dynamics [156]. The radiance sensitivity of the SWIR wavelength band regarding the blackbody temperature is much higher than that of NIR, as well as medium-wave and long-wave infrared imagery cameras. Lough et al. [156] captured the fast melt pool dynamics critical to the microstructure formation of SS304 LPBF-printed parts. The thermal features for each voxel for spatial and temporal domains were extracted using SWIR imaging during the LPBF printing process. The thermal features extracted from the SWIR data for each voxel could indicate whether the voxel contains pore defects. SWIR tracked the thermal history of different voxels during the LPBF process to determine the location and characteristics of defects in another study [157].

Single-camera two-wavelength imaging pyrometry (STWIP) systems utilize a high-speed camera to monitor melt pool dynamics and estimate pool morphology and temperature. In STWIP systems, the melt pool is imaged at two different wavelengths using two photodiodes, and the temperature is estimated using the Imaging Pyrometry method. The estimated temperature is created by extracting the intensity ratio of the melt pool from the STWIP system. STWIP circumvents potential issues caused by multiple camera sensors, such as errors induced by different imaging sensors and the relative location of the melt pool depending on the location of the sensor. Vallabh and Zhao [158] utilized an STWIP system to measure melt pool temperature profiles in NiCr alloy LPBF-printed fatigue bar samples. Disparate temperature profiles in the fatigue bars could indicate potential process anomalies or part defects. An investigation to estimate the melt pool temperature, morphology, and intensity profiles of IN718 LPBF-printed specimens using STWIP was reported [159]. The melt pool temperature signatures collected from the STWIP system were correlated with ex situ microscopy-characterized melt pool depths and average grain lengths. The fusion defects were not observed in the tracks comparing the optical microscopy imaging and STWIP data (see Figure 28). Zhang et al. [160] mapped the STWIP-measured melt pool to detect process anomalies and part defects in IN718 LPBF-printed specimens.

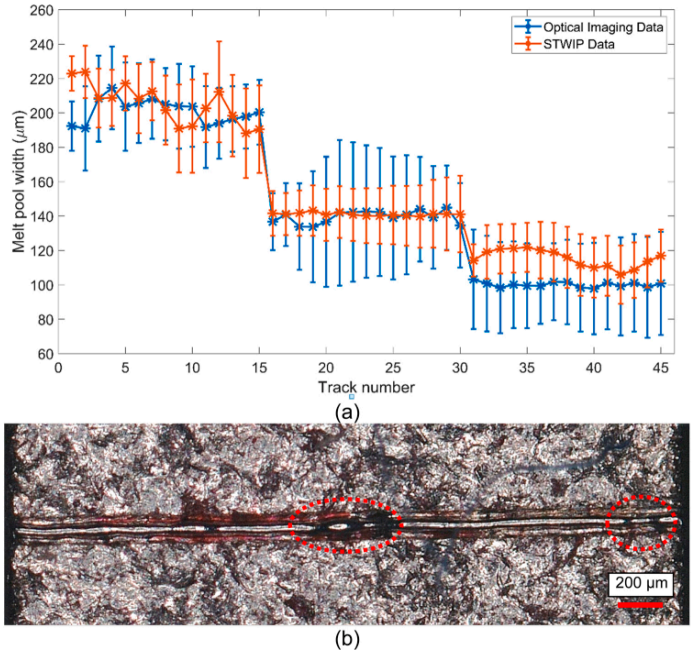

Figure 28. Example provided by [159] of (**a**) a comparison between the melt pool width of the STWIP coaxial camera and optical imaging and (**b**) the single-track with process defects (highlighted).

Infrared pyrometer sensors (IPS) monitor light emitted from the LPBF melt pool and associate specific signatures with certain printing defects. Infrared pyrometer sensors have a fast response time and are dependably repeatable. It is a non-destructive and physically small sensor. However, they are affected by smoke and dust particles. IR pyrometer and photodiode sensors captured the SS316L melt pool thermal emission wavelengths [161]. The thermal signatures obtained through the IR pyrometer correspond to various melt pool modes and can hint towards pore formations and predict defect creation. Duong et al. [162] collected pyrometry measurements during the LPBF printing process of Inconel. A correlation between the pyrometer signal and pore distribution was established, and a probability curve for a given pyrometer signal was derived. Kozjek et al. [163] estimated the melt pool temperature of the AlSi10Mg LPBF-printed part by capturing thermal emission Planck (TEP) process signatures.

The individual TEP signatures were obtained using two photodiodes to collect two light intensity measurements. A system monitored the LPBF printing process of SS316L single tracks, increasing laser power and velocity using high-speed infrared diode-based pyrometry optical imaging signals [98]. The pyrometry signal showed distinct signatures of conduction-to-keyhole mode transitions. A probability correlation predicting pore formation was derived.

Differential scanning calorimeters (DSC) are thermoanalytical devices that measure a material's specific heat capacity change. DSC measures the changes in heat flow (exothermic or endothermic) during metal alloys' heating or cooling processes. These measurements determine the thermodynamic temperatures associated with phase transitions such as solidification and melting [164]. DSC is considered relatively inexpensive but reproducibly difficult. Regarding LPBF printing, DSC has been used to quantify phase transformation temperatures, behaviors, and solidification temperature ranges. The solidification phase change behavior of the printed alloy observed by DSC can hint toward cracking phenomena [165]. The observed undercooling of the alloy powder using a differential DSC was correlated with specific inoculation variants, such as cracks. At the lowest undercooling scenarios, the fewest number of cracks were observed. Chen et al. [61] utilized DSC to determine the phase transformation temperatures of as-fabricated TiNi LPBF-printed samples. The phase transformation temperature was shown using DSC to be significantly affected by the alloy's proportion of Ti and Ni elements.

The Ni element was reported to be disproportionately lost due to the melting process, producing a martensitic transformation temperature difference. Guo et al. [62] similarly investigated the Ni evaporation occurring during the LPBF printing process of NiTi alloys using DSC. The resulting precipitation, dislocations, and internal stresses concerning the phase transformation temperature were also observed. Another study compared DSC measurements with SEM microstructure imagery regarding the variation in the solidification microstructure of AlSi10Mg powder, such as microstructure inhomogeneities [166]. Liu et al. [113] measured the STR of an experimental high W-content nickel-based superalloy using DSC. It was observed that solidification cracking always occurred in the fragile mushy zone where the liquid and solids coexist. This observation concluded that a decreased solidus temperature leads to the formation of low-melting-point liquid films and increases the tendency for liquid cracking. DSC was used to produce thermograms, pointing to a thermal stability regime and a single sharp endotherm temperature, as shown in Figure 29 [75].

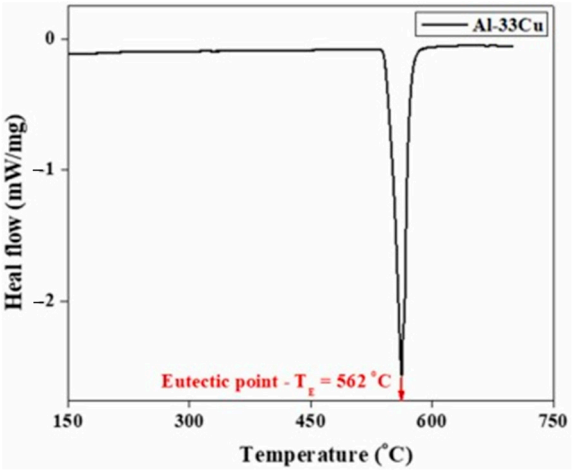

Figure 29. Example provided by [75] for an Al-33Cu LPBF-printed specimen, showing the DSC results identifying the eutectic point of the material.

3.3. Acoustic Techniques

Also referred to as resonance techniques, acoustic techniques detect the excited vibrations in a specimen to assess part quality and detect defects. By collecting the acoustic emissions (AE) generated from the LPBF printing process, the correlation between the anomaly signals and the location can provide insight into the location and size of defects, including internal defects.

Acoustic emission spectroscopy (AES) measures the continuous release of energy from where transient elastic waves are generated in a material. There are two significant components in AE spectroscopy, namely, a fault that is the cause of energy release in the material (event) and the transducer that gathers the data from the produced event. The fault generated from the AE signal appears in high-frequency sound waves [167]. AE spectroscopy has been mainly used for dynamic damage characterization, specifically for crack propagation monitoring. Other internal structural defects can be detected from acoustic signals. AE spectroscopy is a non-destructive technology that can quickly generate valuable data about the location of defects [167]. However, the description generated from the AE cannot accurately describe the size and shape of defects.

Strantza et al. [168] used AE to monitor the fatigue crack growth behavior of LPBF-printed Ti6Al4V components. Two AE broadband "pico" type sensors were attached to the side of the printed specimen. The time delay between the two AE signals and the wave velocity of the material simultaneously were used to determine the crack location. A study performed acoustic resonance testing of SS316L and 6802 T6 aluminum alloy samples to measure the modulus of LPBF-printed lattice samples with a high degree of loose powder adhesion [169]. The samples were excited with a small impact, and a microphone was

used to record the AE signals. The resulting AR test results were reportedly feasible in providing a metric of loose powder adhesion and other structural characteristics. Multiple studies used AE signals to characterize the corrosion behavior of AlSi10mg specimens [170] and monitoring techniques to detect crack formation in a high-strength Al92Mn6Ce2 alloy LPBF-printed component, as shown in Figure 30 [171].

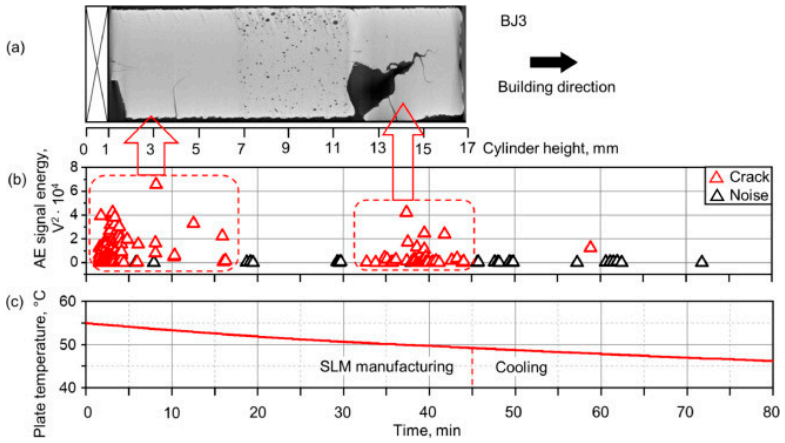

Figure 30. Example provided by [171] showing (**a**) a µ-CT scan of an LPBF-printed part with a large crack, (**b**) AE results indicating the density of cracks, and (**c**) baseplate temperature.

A combination using laser Doppler vibrometry (LDV) with vibrational resonance spectroscopy to develop a laser acoustic resonance spectroscopy (LARS) system was introduced [172]. The LARS system reportedly identified defects rapidly in LPBF cubic components. Acoustic signals generated during the LPBF printing process of SS304 using an equipped nominal microphone attached to the LPBF were collected [173]. Melting states such as overheating, slight overheating, standard, and slight balling in the LPBF printing process are obtained by the relationship between acoustic signals, energy densities, and track formation.

A high-frequency structure-borne sensor was used to detect AE activity associated with cracking. Drissi-Daoudi et al. [174] used a microphone to record the AE signals during the LPBF printing process of SS316L cubic samples. After post-processing, spectrograms were created from the extracted AE signals, revealing the location of defects in the samples. Kononenko et al. [175] collected AE signals during and after the LPBF printing process of Al92Mn6Ce2 cylindrical specimens using a high-temperature structure-borne sensor. The processed AE signal data were used to train various ML algorithms to recognize crack signals.

Fiber Bragg grating (FBG) sensors are one of the most sensitive sensor types for acoustic and pressure wave detection [176]. For FBGs, AE signals are collected through fiber optic sensors, where the strain sensitivity is correlated with the AE measurements. Due to the change in the grating pitch and refractive index through the strain optic effect, the Bragg wavelength exhibits a change when an external strain is applied [177]. FBG sensors are more compact and lighter than standard AE detectors, although they are known to be thermally sensitive, so they have difficulty discriminating wavelength shifts from temperature and strain changes. Wasmer et al. [178] quantified the levels of porosity concentration in SS316L cuboid-shaped samples using a fiber Bragg grating (FBG) optoacoustic sensor. Shevchik et al. [179] used an FBG sensor to detect airborne AE signals generated during the LPBF process. Tubular defects were prevalent at the most considerable energy input, and the lack of fusion defects was dominant at the lowest energy inputs (see Figure 31). Shevchik et al. [180] presented a novel solution for in situ and real-time quality monitoring based on detecting the AE signals emitted during the LPBF printing process.

Nonlinear reverberation spectroscopy (NRS) exploits the amplitude-dependent changes in the resonance frequency of a sample. Once the sample is excited near resonance, the immediate vibration frequency of the decaying reverberation signal decays with decreasing amplitude. The nonlinearity of the material that defects can cause can be determined by

frequency–amplitude dependence. NRS is a non-destructive measurement technique that can rapidly measure AE so that thermal drift is primarily reduced. However, similar to other AE detectors, it cannot describe the defect's characteristics.

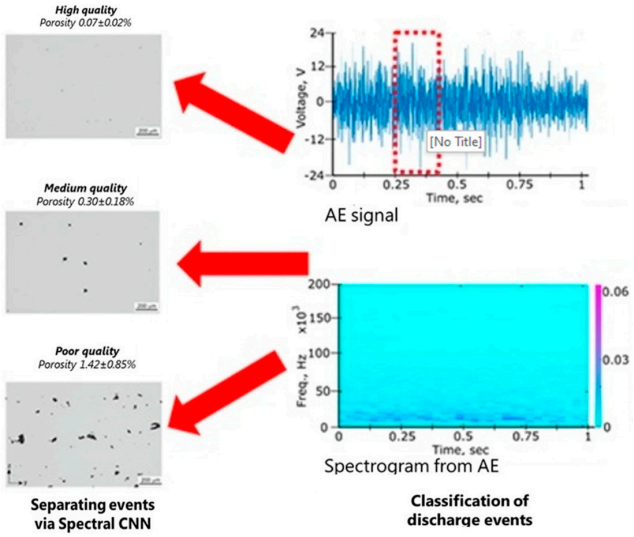

Figure 31. Example of FBG acoustic signals confirming pores in LPBF stainless-steel print (modified from [179]).

Johnson et al. [181] demonstrated the sensitivity of acoustic nonlinearity and loss to small changes in porosity of LPBF-printed custom alloyed Al (0.2 at. % Zn) and commercial Al7075 cylinders. The acoustic signals were generated using non-contacting electromagnetic-acoustic transduction. The relative frequency shift measurements collected from the NRS method exceeded the best-reported precision of nonlinear resonant ultrasound spectroscopy (NRUS) by two orders of magnitude.

3.4. Ultrasonic Techniques

Like acoustic techniques, ultrasonic techniques utilize generated mechanical waves to analyze the quality of LPBF parts. One of the main differences between ultrasonic and acoustic emissions is that for ultrasonic techniques, the ultrasonic waves in the sample are artificially created by forced interaction with an external source. Typically, ultrasonic techniques are performed ex situ.

Immersion ultrasonic (IU) systems are conducted in a water immersion tank with a pulser/receiver and focused transducer to collect routine incidence pulse/echo measurements. A study used IU-measured ex situ ultrasonic backscattering data induced by the microstructure in LPBF-printed samples using a conventional immersion ultrasonic C-scan system and expected frequencies (see Figure 32) [182]. The ultrasonic backscattering data collected from the immersion ultrasonic system effectively detected the flaws of SS316L samples fabricated using LPBF.

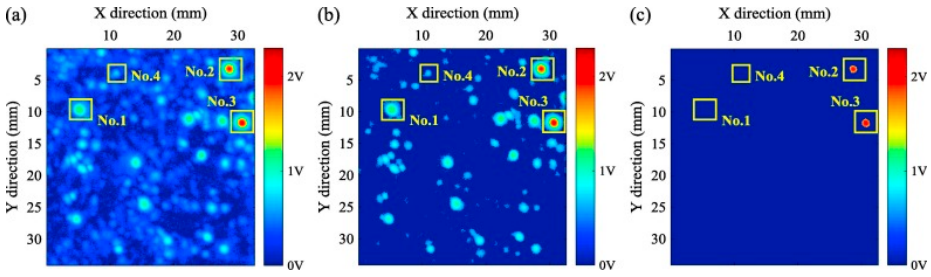

Figure 32. Example provided by [182] showing the immersion ultrasonic C-scan images of an LPBF SS316L printed part segmented by three independent methods: (**a**) time-dependent thresholds, (**b**) 0.5 V fixed threshold, and (**c**) 1.5 V fixed threshold. Lack of fusion and irregular pore defects were observed.

Davis et al. [183] performed IU testing using Parametric© NDT immersion focus probes with the sample mounted inside a plexiglass tank filled with water. Porosities were observed from the IU data, and the average porosity size was about 0.3 mm. Honarvar et al. [184] used linear phased array probes to perform IU experiments to detect artificially embedded defects with various shapes and sizes in AlSi10Mg cubic samples. The IU system could detect defects as small as 0.75 mm, and the IU defect detection capabilities were validated with XCT data.

Laser ultrasonic (LU) systems typically comprise two pulsed lasers and a recording device such as an interferometer or laser Doppler vibrometer (LDV) recording device. The two pulsed lasers trigger the absorption of the incident laser light pulse, which can cause plasma to form directly above the impact point. Once the energy of the plasma reaches a certain level, the expanding plasma is ejected from the surface of the sample and generates ultrasonic waves from the impulsive recoil force that propagates into and along the sample [185]. The interferometer records two pieces of information: (1) a DC monitor signal, which is proportional to the power of the detector beam signal and is a measure of the light reflected from the sample surface, and (2) an AC voltage corresponding to the instantaneous out-of-plane surface displacement. The returning reflected and diffracted ultrasonic wave signals can distinguish the different propagation modes, which can be used to predict the presence of subsurface or surface defects in the area between or adjacent to the two lasers [186]. LU has high reproducibility, fast scanning, and is usable in harsh environments, though it is less sensitive than piezoelectric-based ultrasonic inspection systems. Another challenge the LU system has is that ultrasonic waves' generation efficiency depends on the material's absorption properties.

Additionally, laser safety precautions are necessary. Using a laser ultrasonic system, manually introduced subsurface and surface-breaking micro-defects of LPBF metallic samples were successfully detected [150]. Everton et al. [185,186] investigated the capabilities of LU techniques to detect manufactured subsurface defects in Ti6Al4V LPBF samples. At various depths, subsurface porosities and spherical voids below the surface were successfully detected using LU.

Cerniglia et al. [153] compared the inspection capabilities of LU and laser thermography on IN 600 LPBF samples. Flaws were purposefully created to establish the sensitivity to detect defects. LU effectively detected the typical micrometric defects of AM products. The B-scan images allowed an accurate evaluation of the flaw's location, size, and depth. Liu et al. [187] utilized a laser ultrasonic technique to detect defects in LPBF-printed NiTi-based alloy samples. Results and validation of the ultrasonic data using XCT indicated that the pulsed laser-generated ultrasonic waves were sensitive to internal defects, and thus, LU testing can identify certain defects at the sub-millimeter level (Figure 33).

Hayashi et al. [188] examined an LU method for detecting subsurface defects in an LPBF aluminum alloy flat plate with artificial defects. Subsurface circular defects could be detected for diameters below 1 mm that were undetectably small from previous studies. Chen et al. [189] proposed an ultra-fast LU imaging method to monitor the LPBF process efficiently. A multi-circle combined scanning strategy and defect location algorithm were constructed to improve detection efficiency. A surface wave focusing algorithm (SWFA) was established to solve the low signal-to-noise ratio (SNR) problem induced by rough surface signals. The scanning efficiency of single-layer inspection was reportedly improved by more than 300% compared with the C-scan imaging method.

Pulsing ultrasonic (PU) systems collect ultrasonic waves through pulser-receivers, which generate electrical excitations in a transducer to create an ultrasound pulse-echo. Pulsing ultrasonic systems are non-destructive and highly sensitive, allowing for the detection of minimal flaws and high accuracy in determining the depths of internal flaws. However, pulsing ultrasonic systems cannot accurately estimate defects' orientation, size, nature, and shape. Slotwinski et al. [190] utilized a pulser-receiver to cause a shock-impulse excitation in CoCr LPBF-printed samples.

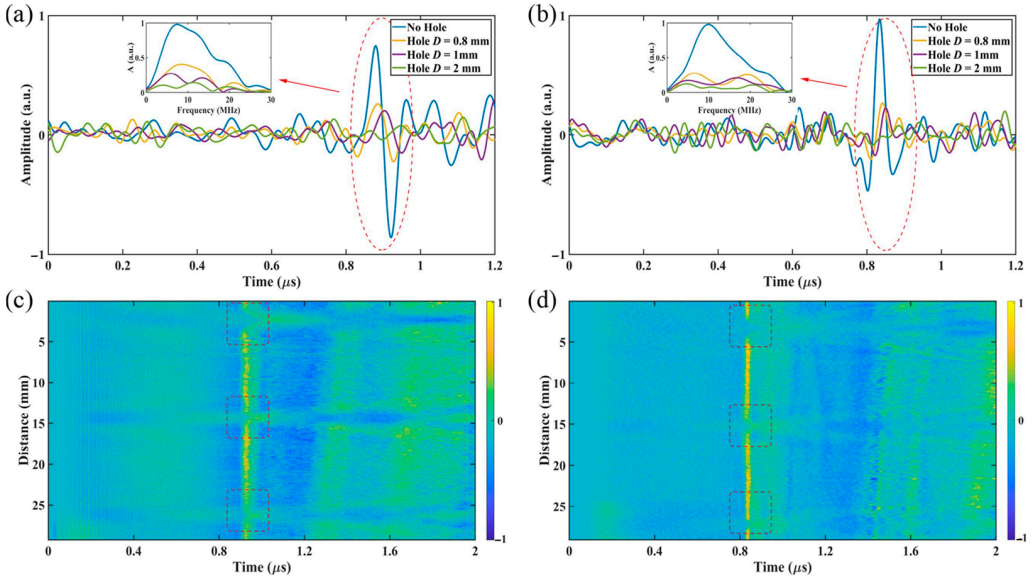

Figure 33. Example provided by [187] showing the LU defect detection results of the LPBF Ni alloy sample (**a**,**c**) and the LPBF Ti alloy sample (**b**,**d**).

The ultrasonic contact pulse-echo velocity measurement method detected minor changes in the porosity concentration, hinting at the ability to detect process deviations such as pore defects in situ. Ladewig et al. [191] used ultrasonic testing to identify the lack of fusion defects of LPBF-printed parts, as shown in Figure 34. Though the ultrasonic method used to generate the scan images was not mentioned, the data was assumed to be generated using a pulse receiver.

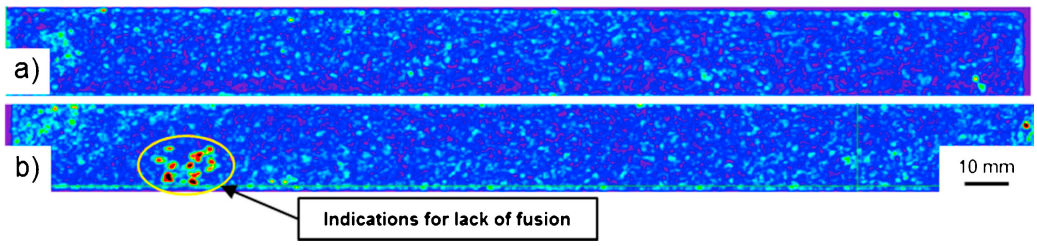

Figure 34. Pulsing ultrasonic results of an LPBF-printed specimen showing a lack of fusion locations for (**a**) 65 m^3/h shielding gas flow rate and (**b**) 32.5 m^3/h shielding gas flow rate [191].

Roy et al. [192] presented an ultrasound measurement of the segmental temperature distribution (US-MSTD) method for evaluating the microstructural heterogeneities and spatial variabilities of mechanical properties in LPBF-printed cylindrical 31 AL aluminum alloy samples. The segmental speed of sound in the sample was collected using a square wave pulse/receiver. The excitation pulse was sent to an ultrasonic transducer coupled to the flat base of the sample. The results obtained from the ultrasound were validated using XCT. Kim et al. [193] studied the dependence of ultrasonic phase velocity on the defect formation of LPBF SS316L components by varying the hatch spacing. A pulse receiver was attached to the sample surface to generate the ultrasonic phase velocity. Lamb et al. [92] measured the ultrasonic sound waves of SS316L LPBF-printed components using a pulser/receiver to recognize the spalling response loaded in different scanning orientations. Raffestin et al. [194] utilized a pulse echo configuration and 10 MHz ultrasonic wave to determine the part quality of a 100Cr6 LPBF-printed part, determining the location of intentionally-created defects. Positives: non-destructive. Negatives: high sensitivity allows for the detection of minor flaws and high accuracy in determining the depth of internal flaws; negatives: cannot accurately estimate the size, orientation, and shape of the defect; cleaning and removing beforehand prep.

Resonant ultrasound spectroscopy (RUS) is a measuring technique to quantify the resonance frequency of a material sample following a mechanical excitation [195]. RUS utilizes the excitation of the elastic stationary wave frequency inherent to a given material to determine the elastic tensor of the material and ultimately analyze part quality. Deviation from the natural frequency can indicate heterogeneities, such as part defects. The RUS technique can obtain the entire elastic tensor from a single crystal sample in a single rapid measurement [196], allowing for relatively fast, contact-free measurements. RUS local resonance behavior data depends on the specimen's local mechanical properties, often requiring assisting technologies to determine the exact locations of defects. Garlea et al. [197] studied the elastic mechanical properties of LPBF-fabricated SS316L samples using RUS. Spectra characteristics obtained from the RUS results showed that the first frequency peak splits and the separation behavior become consistent with the creation of undesired texture and inhomogeneous porosity distributions in part. Bozek et al. [198] investigated the utility of nonlinear RUS (NRUS) to predict fatigue life in cylindrical Ti6Al4V LPBF-printed samples. NRUS was reported to be most sensitive to defects close to the displacement nodes and least sensitive to defects close to the strain nodes.

McGuigan et al. [195] investigated the feasibility of RUS for inspecting complex AM lattice structures with varying numbers of missing struts. Differences between pristine and defective lattices were distinctly identified using RUS. Rossin et al. [199] utilized RUS to analyze SB-CoNi-10C LPBF specimen part quality. EBSD texturing results were quantitatively in agreement with RUS results. Bourdais et al. [200] investigated the viability of RUS in predicting porosities in the AlSi7Mg0.6 LPBF-printed part. The RUS results successfully indicate the presence of a lack of fusion porosities.

Phased array ultrasonic testing (PAUT) is a technique that can transmit and receive ultrasonic wave information independently at different times using multi-element transducers. PAUT reportedly allows for reduced inspection times and can increase ultrasonic testing reliability and sensitivity [201]. According to the literature, bulk ultrasonic wave data from ultrasonic probes can be collected using the total focusing method (TFM), plane wave imaging (PWI), or their Fourier-domain counterparts. In the PAUT process of LPBF part defects, the extracted ultrasonic data can be converted to 2D images, which can be used to detect defects. PAUT has a fast inspection rate, an excellent repeatability factor, and is highly effective in corrosion detection, though it is considered one of the more difficult and complex ultrasonic testing equipment to operate.

Additionally, PAUT is not advised for thin shell structures due to the presence of dead zones that can produce interface distortions of the image [202]. Stratoudaki et al. [203] detected defects in aluminum LPBF components using a laser-induced phased array (LIPA) technique. The LIPA technique detected cylindrical defects (0.5 mm or less in diameter and as deep as 26 mm on the sample surface). Honarvar et al. [184] used a high-frequency PAUT to evaluate the part quality of a cubic AlSi10Mg sample fabricated using LPBF with intentional defects. XCT was used to validate the PAUT-produced data, and it showed excellent agreement, indicating that almost all artificial defects in the test sample were detected. Allam et al. [202] utilized PAUT to detect defects in thick parts fabricated by LPBF, as shown in Figure 35. Practical defects, such as cylindrical lack of fusion defects, were generated by reducing the laser power at prespecified locations. For thin curved components, spatiotemporal guided waves were generated using piezoelectric transducers and measured using a scanning LDV. Cylindrical defects in the thin, curved part were detected and imaged using root mean square wavefield averaging. The defect's shape and density detected using PAUT were verified using optical microscopy and XCT.

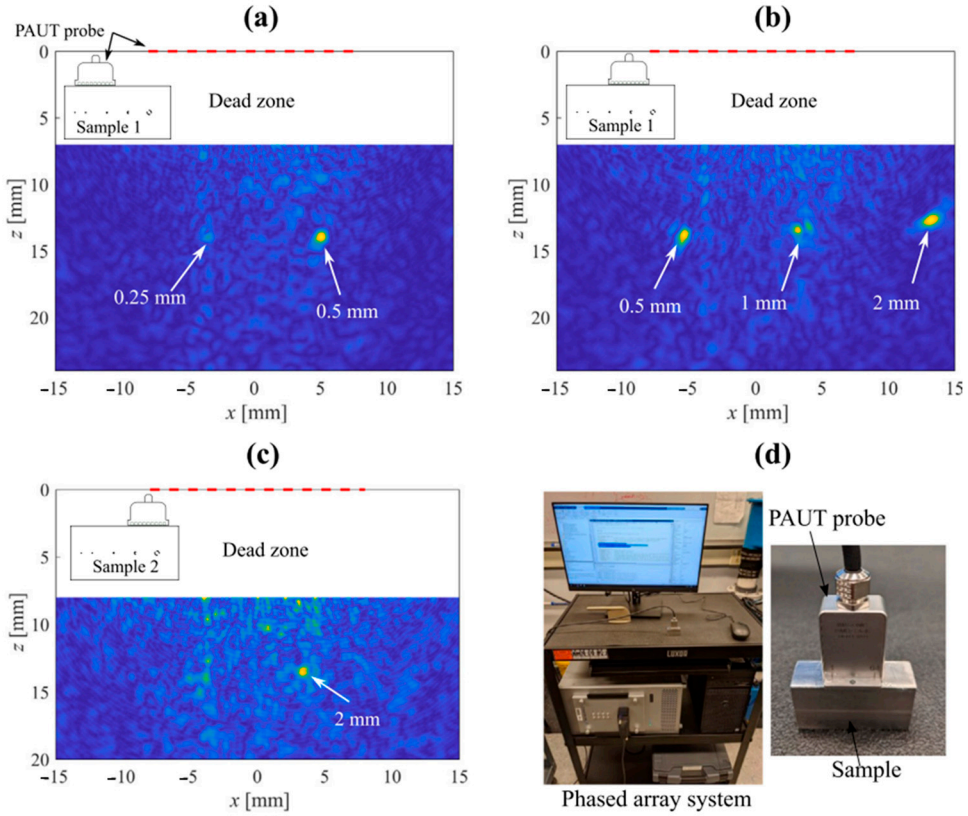

Figure 35. Example of PAUT probe data provided by [202] showing experimental results for (**a**) 0.25 mm and 0.5 mm defects in LPBF sample 1, (**b**) 0.5 mm, 1 mm, and 2 mm defects in LPBF sample 1, (**c**) 2 mm defect in LPBF sample 2, and (**d**) the PAUT experimental setup.

3.5. Miscellaneous Techniques

Many other techniques have been employed to determine the part quality and quantify defect characteristics in LPBF-printed parts. These include using electromagnetic induction, cantilevered probes, and gas pycnometers

Eddy current testing (ECT) detects and characterizes subsurface and surface defects of metallic components using electromagnetic induction. A magnetic field at a specified excitation frequency excites eddy currents in the metallic object. The EC flow pattern is perturbed in the presence of a defect, appearing as localized magnetic anomalies [203].

EC testing is ideal for testing surface flaws, has very high accuracy in conductivity measurements, and requires very little sample preparation. However, EC testing cannot detect defects parallel to the surface and is considered unsuitable for complex geometries. Du et al. [204] performed a feasibility test on an EC testing system's subsurface defect detection capability. The EC method successfully detected subsurface defects in Ti6Al4V AM parts. The direct laser deposition (DLD) method was used to prepare the specimens, though EC in defect detection applies to LPBF.

Goodall et al. [205] minimized EC losses in a high-silicon electrical steel (Fe-6.5%wt. Si) fabricated using LPBF to reduce defect population. Various cross-section designs were produced and analyzed regarding the EC losses. Various defects, such as lack of fusion, cracking, excessive surface roughness, electrical shorting between areas that should be isolated, and gas/keyhole porosities, were highlighted regarding unintended EC pathway circulation.

Atomic force microscopy (AFM) probes operate using a supported, tiny spring-like cantilever with a tip on one end and a piezoelectric element to oscillate the cantilever at its eigenfrequency on the other end. A detector located very close above the cantilever detects any deflection or motion of the cantilever. A 3D image of the topographical shape of the sample surface can be detected at a high resolution from the reaction of the probe to the forces the sample imposes on it. The AFM does not include lenses or beam irradiation, eliminating

spatial resolution limitations caused by diffraction and aberration. The resolution has been noted to be higher than SEM and comparable with TEM, though AFM can only perform a single scan, which can be time-consuming and is affected by thermal drift and the hysteresis of the piezoelectric material. The forces applied to the probe over the sample are a function of their mutual separation and are used to measure its mechanical properties. Lodhi et al. [146] utilized AFM to characterize the surface roughness of an SS316L LPBF-printed surface, as shown in Figure 36. Mussatto et al. [95] determined the surface topology of various hatching methods for SS316L LPBF-printed parts using AFM.

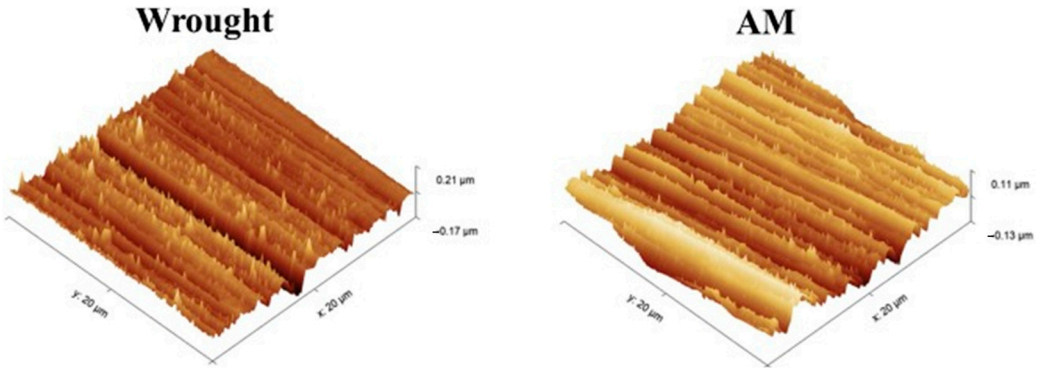

Figure 36. AFM-generated surface roughness profiles comparing SS316 wrought and LPBF-printed samples [146].

Gas pycnometers (GP) are devices used to measure the density of solid samples. A pathway connects two gas pycnometer chambers with a valve. The first chamber is a gas-tight chamber with a pressure transducer to house the solid sample, and the second chamber is a reference chamber with a fixed internal volume. A valve pushes pressurized gas into the first chamber and passes into the second chamber via the connection with a valve. The second chamber contains a vent valve. The sample volume can be directly estimated from the chamber volume, reference volume, and pressure ratios between the two chambers. The bulk relative density of LPBF-printed parts can be calculated using gas pycnometers. A gas pycnometer can help indicate whether the sample density is within the expected density range, which can help justify whether the part is fully dense or has significant porosities. Gas pycnometry has been used alongside the Archimedean method to determine the bulk density of LPBF-printed parts [90,92]. Positives of a gas pycnometer include high volumetric measurement accuracy, high reproducibility, and operation in a closed system, which eliminates many external factors. Negatives: It requires significant sample volumes, is challenging to clean and dry, is potentially time-consuming, and is expensive.

Conversion electron Mössbauer spectroscopy (CEMS) is a susceptible method for investigating the surface of complex, highly absorbing samples. Mossbauer spectroscopy examines iron's valence state, which cannot be differentiated using EPMA. CEMS is a non-destructive technology that can provide high-resolution data; however, it is known to be vibrationally sensitive and requires cryogenic conditions. Gainov et al. [97] investigated corrosion-resistant alloy 800H steel samples fabricated using LPBF, as shown in Figure 37. CEMS proved that phase separation does not occur during the LPBF process and that the oxidation of the steel does not cause hot cracking in the samples.

Neutron diffraction (ND) uses an accelerator to produce an incident neutron beam that can create a wavelength spectrum. The diffracted neutrons can be measured using detector banks. The through-thickness resolution of the specimen can be specified using a set of radial collimators in front of the detectors. Neutron diffraction is more reliable in determining elemental composition than X-ray or electron beam methods and can detect residual stresses beneath the surface of the investigated sample. However, significant energy is required to produce the large number of neutrons needed. Smith et al. [206] used neutron diffraction to measure the longitudinal and transverse residual stresses in pre-

and post-annealed SS316L LPBF parts, as shown in Figure 38. Pant et al. [68] measured bulk residual stresses in IN718 LPBF samples using the neutron diffraction technique. The sensitivity of the measured interplanar distance for stress-free sample strains in the three orthogonal directions could be attributed to the local variation in the microstructure defects.

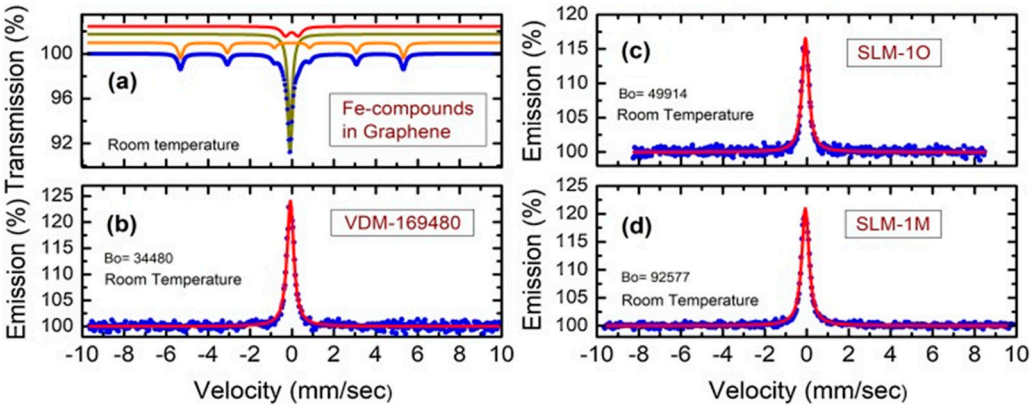

Figure 37. Example of Mössbauer spectrum data provided by [97] showing (**a**) comparison of data mixture of austenite non-magnetic steel (dark-yellow singlet), magnetic steel (orange sextet), and Fe–O oxide (red doublet), (**b**) CEMS spectral data of A800H steel industrial plate, and (**c**,**d**) LPBF-manufactured plates of 1O, and 1M.

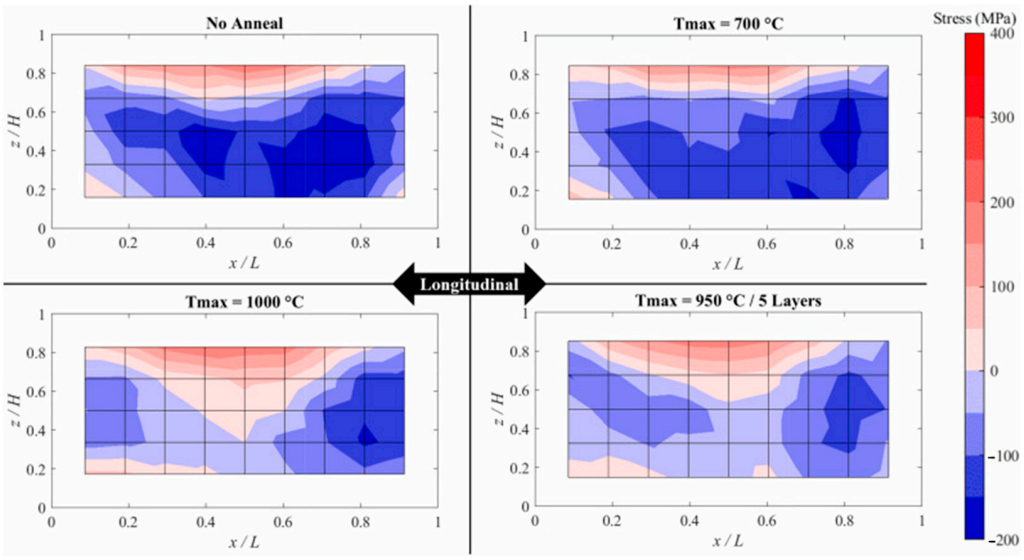

Figure 38. Longitudinal stress map generated using ND along the central longitudinal plane of SS316L LPBF-printed sample [206].

Electrochemical impedance spectroscopy (EIS) is used to analyze the effects of corrosion on the microstructure and electrochemical behavior. The electrochemical value measured at the electrode interface reflects the magnitude of the property, and the concentration of chemical species is measured. The steady-state technique utilizes small signal analysis and probe signal relaxation over various applied frequencies. The corrosion rate is highly dependent on the microstructure, the difference between the constituent phases, and the density of the beta-grain boundaries [206]. Due to the layered structure present in AM, mechanical properties and corrosion resistance differ from those of standard manufacturing. The corrosion resistance of LPBF samples is usually higher than that of standard manufactured parts [206]. EIS is a quick and non-destructive method for analyzing corrosion effects on LPBF-printed microstructures. However, accuracy depends on prior measurements and developed models, which can be pretty complex. Zadeh et al. [207] confirmed using EIS

that LPBF-printed parts have better corrosion performance than EBM due to the higher charge transfer resistance of the LPBF-fabricated Ti6Al4V alloy at all immersion times. Chen et al. [61] showed using EIS that the body fluid resistance (simulated body fluid resistance between the working and the reference electrode) of the LPBF TiNi printed sample is lower than that of the TiNi ingot. Still, the charge transfer resistance (resistance of the electrode reaction) is higher than that of the ingot, showing better corrosion resistance. Cheng et al. [147] investigated the effect of various passivation times on the structure and the properties of the passivation film of an LPBF-printed IN718 sample using EIS. The results imply that as the film formation time increases, the passive film becomes more stable, containing fewer internal defects and better corrosion resistance.

Despite an expansive list of technologies and methods available for LPBF defect detection, there are a myriad of other sensing technologies used that are not elaborated on in this paper. Other sensing technologies used to detect, quantify and characterize LPBF defects include: surface characterization tools (surface profilometers [208], Vickers hardness testers [209] and Rockwell [210] hardness testers), optical imaging technologies (X-ray ptychography (XRP) [211]), thermal sensing technologies (pulsed infrared thermography (PIT) [212], thermoreflectance thermal imaging (TTI) [213] and thermal desorption spectroscopy (TDS) [214]), acoustic and ultrasonic sensing technologies (scanning acoustic microscopy (SAM) [215], spatially resolved acoustic spectroscopy (SRAS) [216], electromagnetic acoustic transducer (EMAT) [217], and advanced ultrasonic backscatter technique (AUBT) [218]) and other miscellaneous sensing techniques (Mott–Schottky (M-S) [219], Raman spectroscopy (RS) [220], electrical resistance tomography (ER) [221], secondary ion mass spectroscopy (SIMS), [222], atomic absorption spectroscopy (AAS) [223], replication metallography (RM) [224], electronic speckle pattern interferometry (ESPI) [225], magnetic force microscopy (MFM) [226], giant magneto resistive (GMR) sensors [227], alternating current potential drop (ACPD) [228], magnetic Barkhausen noise (MBN) [229], and dye penetrant testing (PT), [230]).

Other sensing technologies proven to detect metal welding defects but have yet to be used in LPBF defect detection include X-ray computed laminography (CL), photocurrent spectroscopy (PS), frequency modulated thermography (FMT), micro-laser line thermography (μLLT), micro-laser spot thermography (μLST), Barker code laser infrared thermography (BCLIT), scanning thermal microscopy (SThM), Golay-coded thermal wave imaging (GCTWI), ultrasonic infrared thermography (UIT), magnetic flux leakage testing (MFL), magneto-acousto-electrical tomography (MAET), tunnel magneto resistive (TMR) sensors, lateral shearing interferometer (LSI), digital shearography (DS), alternating current field measurement (ACFM) method, magnetic particles testing (MT), metal magnetic memory testing (MMM), bacterial cells testing (BCT) ,and quantum dots fluorescent-penetrant testing (Qdots) [231].

4. Recommended Sensing Technologies for Defect Types

The aptitude of each explained sensing technology has positives and negatives in its LPBF defect detection capabilities. The impetus for utilizing multiple sensing technologies to identify LPBF defects is that certain sensing technologies excel in detecting specific internal and external defect types, while others excel in determining part chemical compositions or overall density. LPBF part analysis typically involves combinations of destructive and non-destructive technologies to maximize the amount of information on a print quality. Destructive sensing technologies involve techniques that cause irreparable damage to the print surface, thus making subsequent usages of the same sample incapable. Non-destructive sensing technologies are the opposite, allowing for subsequent usage of the same sample for analysis. This section explains the capabilities of each described sensing technology from Section 3 to detect the LPBF defect types reported in Section 2 for optical, thermal, acoustic, ultrasonic, and other miscellaneous techniques. Though many references are available to identify a sensing technology's capability to detect and analyze a specific defect, only single references are provided in Tables 6–10 for each technology–defect connection

in order of the provided checkmarks. The sample destructive technique or technology is marked with an asterisk in the tables' header.

4.1. Recommended Optical Sensing Techniques for Defect Types

Optical electron source techniques can detect and observe all presented defect types. Alone, SEM technologies reportedly detect all defects except for vaporization defects. SEM is the only current reported technology to detect balling, surface roughness, and denudation surface-quality defects. Surface oxidation defects are detected by all-optical techniques using an electron source except EBSD, with SEM, TEM, and EPS producing images of surface oxidation behavior and XPS and EPMA producing surface chemical composition hinting toward surface oxidation. LOF porosities can be detected using SEM and TEM, while gas porosities can be captured using SEM. Keyhole porosities can be visually captured using SEM and TEM, while EPMA quantitative chemical analysis maps can hint at keyhole porosity formations. Liquation cracking can be observed using SEM and chemically determined using EBSD and EDS. Solidification cracking can be observed using SEM and chemically determined using EBSD. Delamination behavior can be visually observed using SEM and chemically confirmed using EDS (EDX). Optical techniques using an X-ray source can detect almost all defects. XCT can observe vaporization surface-quality defects and all microstructural defects. Liquation cracking can be observed using XCT. XRD can hint toward surface oxidation and surface roughness defects. XRD can also hint towards gas porosities and delamination. Optical techniques using a visible light source are reported to detect and observe all presented defect types.

Balling defects can be visually detected using OM and CLSM. OM can also detect surface oxidation and vaporization. Surface roughness and denudation can be observed using OM, CLSM, and DSLR. OM and CLSM can observe LOF porosities. OM can observe gas and keyhole porosities. Liquation and solidification cracking can be detected using OM and DIC. Delamination can be visually detected using CLSM and DSLR. Optical techniques using other sources are reported to detect some surface-quality defects. Surface oxidation can be detected using OES and APT. Surface roughness can be detected using APT. Tables 6 and 7 summarize the possible sensing technologies for each defect using optical techniques.

4.2. Recommended Thermal Sensing Techniques for Defect Types

Thermal techniques have been reported to detect many defects, excluding surface oxidation, gas porosities, and delamination. Balling defects can be detected using IRTC. STWIP can detect surface roughness. Denudation and vaporization defects can be reportedly detected using TIC. LOF porosities can be detected using SWIR and SWTIP. Keyhole porosities can be detected using IRTC, SWIR, and IPS. Liquation cracking and solidification cracking can be detected using DSC. Table 8 summarizes the possible sensing technologies for each defect using thermal techniques.

Table 6. Applicability of optical sensing technologies (electron source) to detect LPBF defects.

Defect Type	Defect	SEM	TEM *	EBSD	EDS	XPS	EPMA
Surface-quality defects	Balling [6]	✓					
	Surface oxidation [46,58,65,76,109]	✓	✓		✓	✓	✓
	Surface roughness [50]	✓					
	Denudation [6]	✓					
	Vaporization [67]				✓		
Microstructure defects	LOF porosities [20,61]	✓	✓				
	Gas porosities [20]	✓					
	Keyhole porosities [8,24,57]	✓	✓				✓

Table 6. *Cont.*

Defect Type	Defect	SEM	TEM *	EBSD	EDS	XPS	EPMA
Mech. defects	Liq. cracking [29,64,232]	✓		✓	✓		
	Sol. cracking [29,65]	✓		✓			
	Delamination [44]	✓			✓		

Table 7. Applicability of optical sensing technologies (X-ray, light, and other sources) to detect LPBF defects.

Defect Type	Defect	XCT	XRD	OM	CLSM	DSLR	DIC	OES *	APT *
Surface-quality defects	Balling [12,191]			✓	✓				
	Surface oxidation [11,82,108,128]		✓	✓				✓	✓
	Surface roughness [13,49,91,125,146]		✓	✓	✓	✓			✓
	Denudation [15,16]			✓	✓	✓			
	Vaporization [15,17]	✓		✓					
Microstructure defects	LOF porosities [59,66,191]	✓		✓	✓				
	Gas porosities [20,190,197]	✓	✓	✓					
	Keyhole porosities [98,156]	✓		✓					
Mech. defects	Liq. cracking [29,32,115]	✓		✓			✓		
	Sol. cracking [32,118,190]	✓		✓			✓		
	Delamination [17,33,191]		✓		✓	✓			

Table 8. Applicability of other optical and thermal sensing technologies to detect LPBF defects.

Defect Type	Defect	TIC	IRTC	SWIR	STWIP	IPS	DSC *
Surface-quality defects	Balling [25]		✓				
	Surface oxidation [82,128]			✓	✓		
	Surf. roughness [158]				✓		
	Denudation [150]	✓					
	Vaporization [150]	✓					
Microstructure defects	LOF porosities [155,159]			✓	✓		
	Keyhole porosities [105,154,155]		✓	✓		✓	
Mech. defects	Sol. cracking [165]						✓

4.3. Recommended Acoustic and Ultrasonic Sensing Techniques for Defect Types

Acoustic and ultrasonic techniques have been reported to capture the majority of reported defects. Acoustic techniques can detect surface quality, microstructure, and mechanical defects, while ultrasonic defects can only detect microstructure and mechanical defects. Balling surface-quality defects can be detected using AES and NRS. LOF porosity microstructure defects can be detected using acoustic techniques such as FBG and NRS and all ultrasonic techniques, including IU, LU, PU, RUS, and PAUT. Gas porosities can be detected using IU and LU. Keyhole porosities can be detected using IU. Liquation and solidification cracking can be detected using AES. IU and LU can detect solidification cracking and delamination defects. Table 9 summarizes the possible sensing technologies for each defect using acoustic and ultrasonic techniques.

Table 9. Available ultrasonic sensing technologies to detect LPBF defects.

Defect Type	Defect	AES	FBG	NRS	IU	LU *	PU	RUS	PAUT
Surface-quality defects	Balling [173,181]	✓		✓					
Microstructure defects	LOF porosities [179,181, 182,187,191,200,202]		✓	✓	✓	✓	✓	✓	✓
	Gas porosities [183,187]				✓	✓			
	Keyhole porosities [184]				✓				
Mech. defects	Liq. cracking [168]	✓							
	Sol. cracking [170,184,189]	✓			✓	✓			
	Delamination [184,188]				✓	✓			

4.4. Recommended Miscellaneous Sensing Techniques for Defect Types

Other miscellaneous techniques can detect many of the mentioned defects. Surface oxidation can be detected using CEMS and EIS. AFM and EIS can be used to detect surface roughness. LOF porosities can be detected using ECT and ND. Keyhole porosities can be detected using ECT. ECT can be used to detect solidification cracking. Table 10 summarizes the possible sensing technologies for each defect using the mentioned miscellaneous techniques.

Table 10. Available miscellaneous sensing technologies to detect LPBF defects.

Defect Type	Defect	ECT	AFM	GP	CEMS	ND	EIS
Surface-quality defects	Surface oxidation [61,97]				✓		✓
	Surface roughness [146,207]		✓				✓
Microstructure defects	LOF porosities [68,205]	✓				✓	
	Keyhole porosities [205]	✓					
Mech. defects	Sol. cracking [205]	✓					

5. Conclusions

The integrative potential of LPBF-printed parts for various innovative applications depends upon the robustness and infallibility of the part quality. Eliminating or sufficiently reducing factors contributing to the formation of defects is an integral step to achieving satisfiable part quality. Many advanced sensing, modeling, and artificial intelligence techniques have proven effective in characterizing, detecting, and monitoring defects. Often, combinations of sensing techniques are applied to deepen the understanding of the investigated phenomena. The AM-LPBF method continues to innovate and provide solutions to part quality issues through these advanced sensing techniques.

Author Contributions: Conceptualization, D.G., S.W. and A.A.; investigation, S.W. and A.A.; writing—original draft preparation, S.W. and A.A.; writing—review and editing, D.G. and S.W.; project administration, D.G.; funding acquisition, D.G. All authors have read and agreed to the published version of the manuscript.

Funding: This work was supported by the Center for Advanced Energy Studies (CAES) business development funds as part of Idaho National Laboratory under the Department of Energy (DOE) Idaho Operations Office (an agency of the US Government) Contract DE-AC07-05ID145142.

Institutional Review Board Statement: Not applicable.

Informed Consent Statement: Not applicable.

Data Availability Statement: Not applicable.

Conflicts of Interest: The authors declare no conflicts of interest.

References

1. Herzog, D.; Seyda, V.; Wycisk, E.; Emmelmann, C. Additive manufacturing of metals. *Acta Mater.* **2016**, *117*, 371–392. [CrossRef]
2. Cai, C.; Zhou, K. Chapter 7-Metal additive manufacturing. In *Digital Manufacturing: The Industrialization of Art to Part 3D Additive Printing*; Elsevier: Amsterdam, The Netherlands, 2022; pp. 247–298. [CrossRef]
3. Malekipour, E.; El-Mounayri, H. Common defects and contributing parameters in powder bed fusion AM process and their classification for online monitoring and control: A review. *Int. J. Adv. Manuf. Technol.* **2018**, *95*, 527–550. [CrossRef]
4. Qiu, C.; Panwisawas, C.; Ward, M.; Basoalto, H.C.; Brooks, J.W.; Attallah, M.M. On the role of melt flow into the surface structure and porosity development during selective laser melting. *Acta Mater.* **2015**, *96*, 72–79. [CrossRef]
5. Shen, Y.F.; Gu, D.; Pan, Y.F. Balling Process in Selective Laser Sintering 316 Stainless Steel Powder. *Key Eng. Mater.* **2006**, *316*, 315–316. [CrossRef]
6. Yakout, M.; Elbestawi, M.A.; Veldhuis, S.C. A study of thermal expansion coefficients and microstructure during selective laser melting of invar 36 and stainless steel 316L. *Addit. Manuf.* **2018**, *24*, 405–418. [CrossRef]
7. Olakanmi, E.O.; Dalgarno, K.W.; Cochrane, R.F. Laser sintering of blended Al-Si powders. *Rapid Prototyp. J.* **2012**, *18*, 109–119. [CrossRef]
8. Aboulkhair, N.T.; Everitt, N.M.; Ashcroft, I.; Tuck, C. Reducing porosity in AlSi10Mg parts processed by selective laser melting. *Addit. Manuf.* **2014**, *1–4*, 77–86. [CrossRef]
9. Felix, S.; Majumder, S.R.; Mathews, H.K.; Lexa, M.; Lipsa, G.; Ping, X.; Roychowdhury, S.; Spears, T. In situ process quality monitoring and defect detection for direct metal laser melting. *Sci. Rep.* **2022**, *12*, 8503. [CrossRef]
10. Simonelli, M.; Tuck, C.; Aboulkhair, N.T.; Maskery, I.; Ashcroft, I.; Wildman, R.D.; Hague, R. A study on the laser spatter and the oxidation reactions during selective laser melting of 316l stainless steel, Al-Si10-Mg, and Ti-6Al-4V. *Metall. Mater. Trans.* **2015**, *46*, 3842–3851. [CrossRef]
11. Li, Y.; Yang, H.; Lin, X.; Huang, W.; Li, J.; Zhou, Y. The influences of processing parameters on forming characterizations during laser rapid forming. *Mater. Sci. Eng.* **2003**, *360*, 18–25. [CrossRef]
12. Chowdhury, S.; Yadiah, N.; Prakash, C.; Ramakrishna, S.; Dixit, S.; Gupta, L.R.; Buddhi, D. Laser powder bed fusion: A state-of-the-art review of the technology, materials, properties & defects, and numerical modeling. *J. Mater. Res. Technol.* **2022**, *20*, 2109–2172. [CrossRef]
13. Nezhadfar, P.D.; Shrestha, R.; Phan, N.; Shamsaei, N. Fatigue behavior of additively manufactured 17-4 PH stainless steel: Synergistic effects of surface roughness and heat treatment. *Int. J. Fatigue* **2019**, *124*, 188–204. [CrossRef]
14. Gusarov, A.; Yadroitsev, I.; Bertrand, P.; Smurov, I. Model of radiation and heat transfer in laser-powder interaction zone at selective laser melting. *J. Heat Transf.* **2009**, *131*, 072101. [CrossRef]
15. Matthews, M.J.; Guss, G.; Khairallah, S.A.; Rubenchik, A.M.; Depond, P.J.; King, W.E. Denudation of metal powder layers in laser powder bed fusion. *Acta Mater.* **2016**, *114*, 33–42. [CrossRef]
16. Yadroitsev, I.; Bertrand, P.; Smurov, I. Parametric analysis of the selective laser melting process. *Appl. Surf. Sci.* **2007**, *253*, 8064–8069. [CrossRef]
17. Guo, Q.; Zhao, C.; Escano, L.I.; Young, Z.; Xiong, L.; Fezzaa, K.; Everhart, W.; Brown, B.; Sun, T.; Chen, L. Transient dynamics of powder spattering in laser powder bed fusion additive manufacturing process revealed by in-situ high-speed high energy x-ray imaging. *Acta Mater.* **2018**, *151*, 169–180. [CrossRef]
18. Cao, X.; Jahazi, M.; Immarigeon, J.; Wallace, W. A review of laser welding techniques for magnesium alloys. *J. Mater. Process. Technol.* **2006**, *171*, 188–204. [CrossRef]
19. Rombout, M.; Kruth, J.P.; Froyen, L.; Mercelis, P. Fundamentals of Selective laser melting of alloyed steel powders. *CIRP Ann.* **2006**, *55*, 187–192. [CrossRef]
20. Eliasu, A.; Czekanski, A.; Boakye-Yiadom, S. Effect of laser powder bed fusion parameters on the microstructural evolution and hardness of 316L stainless steel. *Int. J. Adv. Manuf. Technol.* **2021**, *113*, 2651–2669. [CrossRef]
21. Heiden, M.J.; Deibler, L.A.; Rodelas, J.M.; Koepke, J.R.; Tung, D.J.; Saiz, D.J.; Jared, B.H. Evolution of 316L stainless steel feedstock due to laser powder bed fusion process. *Addit. Manuf.* **2019**, *25*, 84–103. [CrossRef]
22. Tucho, W.M.; Lysne, V.H.; Austbø, H.; Sjolyst-Kverneland, A.; Hansen, V. Investigation of effects of process parameters on microstructure and hardness of SLM manufactured SS316L. *J. Alloys Compd.* **2018**, *740*, 910–925. [CrossRef]
23. Gordon, J.V.; Narra, S.P.; Cunningham, R.W.; Liu, H.; Chen, H.; Suter, R.M.; Beuth, J.L.; Rollett, A.D. Defect structure process maps for laser powder bed fusion additive manufacturing. *Addit. Manuf.* **2020**, *36*, 101552. [CrossRef]
24. Liu, Y.J.; Li, S.J.; Wang, H.L.; Hou, W.T.; Hao, Y.L.; Yang, R. Microstructure, defects and mechanical behavior of beta-type titanium porous structures manufactured by electron beam melting and selective laser melting. *Acta Mater* **2016**, *113*, 56–67. [CrossRef]
25. Yang, J.; Schlenger, L.M.; Nasab, M.H.; Petegem, S.V.; Marone, F.; Logé, R.E.; Leinenbach, C. Experimental quantification of inward Marangoni convection and its impact on keyhole threshold in laser powder bed fusion of stainless steel. *Addit. Manuf.* **2024**, *84*, 104092. [CrossRef]
26. Shiva, S.; Palani, I.A.; Mishra, S.K.; Paul, C.P.; Kukreja, L.M. Investigations on the Influence of Composition in the Development of Ni-Ti Shape Memory Alloy Using Laser Based Additive Manufacturing. *Opt. Laser Technol.* **2015**, *69*, 44–51. [CrossRef]
27. Brennan, M.C.; Keist, J.S.; Palmer, T.A. Defects in Metal Additive Manufacturing Processes. *J. Mater. Eng. Perform.* **2021**, *30*, 4808–4818. [CrossRef]
28. Simson, T.; Emmel, A.; Dwars, A.; Böhm, J. Residual stress measurements on AISI 316L samples manufactured by selective laser melting. *Addit. Manuf.* **2017**, *17*, 183–189. [CrossRef]

29. Chen, Y.; Zhang, K.; Huang, J.; Hosseini, S.R.E.; Li, Z. Characterization of heat affected zone liquation cracking in laser additive manufacturing of Inconel 718. *Mater. Des.* **2016**, *90*, 586–594. [CrossRef]
30. Marchese, G.; Basile, G.; Bassini, E.; Aversa, A.; Lombardi, M.; Ugues, D.; Fino, P.; Biamino, S. Study of the microstructure and cracking mechanisms of Hastelloy X produced by LPBF. *Materials* **2018**, *11*, 106. [CrossRef]
31. Chen, Y.; Lu, F.; Zhang, K.; Nie, P.; Hosseini, S.R.E.; Feng, K.; Li, Z. Dendritic microstructure and hot cracking of laser additive manufactured Inconel 718 under improved base cooling. *J. Alloys Compd.* **2016**, *670*, 312–321. [CrossRef]
32. Narasimharaju, S.R.; Zeng, W.; See, T.L.; Zhu, Z.; Scott, P.; Jiang, X.; Lou, S. A comprehensive review on laser powder bed fusion of steels: Processing, microstructure, defects and control methods, mechanical properties, current challenges, and future trends. *J. Manuf. Process.* **2022**, *75*, 375–414. [CrossRef]
33. Kempen, K.; Thijs, L.; Vrancken, B.; Buls, S.; Humbeeck, J.V.; Kruth, J.-P. Producing crack-free, high-density M2 HSS parts by selective laser melting: Pre-heating the baseplate. In Proceedings of the 2013 International Solid Freeform Fabrication Symposium, Austin, TX, USA, 12–14 August 2013.
34. DebRoy, T.; Wei, H.L.; Zuback, J.S.; Mukherjee, T.; Elmer, J.W.; Milewski, J.O.; Beese, A.M.; Wilson-Heid, A.; De, A.; Zhang, W. Additive manufacturing of metallic components–Process, structure and properties. *Prog. Mater. Sci.* **2018**, *92*, 112–224. [CrossRef]
35. Ye, D.; Fuh, J.Y.H.; Zhang, Y.; Hong, G.S.; Zhu, K. In situ monitoring of selective laser melting using plume and spatter signatures by deep belief networks. *ISA Trans.* **2018**, *81*, 96–104. [CrossRef]
36. Yang, X.; Li, Y.; Duan, M.-g.; Jiang, W.; Chen, D.; Li, B. An investigation of ductile fracture behavior of Ti6Al4V alloy fabricated by selective laser melting. *J. Alloys Compd.* **2022**, *890*, 161926. [CrossRef]
37. Chen, Y.; Zhu, H.; Zhang, P.; Wang, Z.; Wang, M.; Sha, G.; Lin, H.; Ma, J.; Zhang, Z.; Song, Y.; et al. An exceptionally strong, ductile, and impurity-tolerant austenitic stainless steel prepared by laser additive manufacturing. *Acta Mater.* **2023**, *250*, 118868. [CrossRef]
38. Kong, D.; Dong, C.; Ni, X.; Liang, Z.; Man, C.; Li, X. Hetero-deformation-induced stress in additively manufactured 316L stainless steel. *Mater. Res. Lett.* **2020**, *8*, 390–397. [CrossRef]
39. Kong, D.-c.; Dong, C.-f.; Ni, X.-q.; Zhang, L.; Li, R.-x.; He, X.; Man, C.; Li, X.-g. Microstructure, and mechanical properties of nickel-based superalloy fabricated by laser powder-bed fusion using recycled powders. *Int. J. Miner. Metall. Mater.* **2021**, *28*, 266–278. [CrossRef]
40. Ghosh, A.; Biswas, S.; Turner, T.; Kietzig, A.-M.; Brochu, M. Surface, microstructure, and tensile deformation characterization of LPBF SS316L microstruts micromachined with femtosecond laser. *Mater. Des.* **2021**, *210*, 110045. [CrossRef]
41. Beard, W.; Lancaster, R.; Barnard, N.; Jones, T.; Adams, J. The influence of surface finish and build orientation on the low cycle fatigue behavior of laser powder bed fused stainless steel 316L. *Mater. Sci. Eng. A* **2023**, *864*, 144593. [CrossRef]
42. Huang, G.; Wei, K.; Deng, J.; Liu, M.; Zeng, X. High-power laser powder bed fusion of 316L stainless steel: Defects, microstructure, and mechanical properties. *J. Manuf. Process.* **2022**, *83*, 235–245. [CrossRef]
43. Gokcekaya, O.; Ishimoto, T.; Hibino, S.; Yasutomi, J.; Narushima, T.; Nakano, T. Unique crystallographic texture formation in Inconel 718 by laser powder bed fusion and its effect on mechanical anisotropy. *Acta Mater.* **2021**, *212*, 116876. [CrossRef]
44. Cai, C.; Radoslaw, C.; Zhang, J.; Yan, Q.; Wen, S.; Song, B.; Shi, Y. In-situ preparation and formation of TiB/Ti-6Al-4V nanocomposite via laser additive manufacturing: Microstructure evolution and tribological behavior. *Powder Technol.* **2019**, *342*, 73–84. [CrossRef]
45. Raza, A.; Fiegl, T.; Hanif, I.; Markström, A.; Franke, M.; Körner, C.; Hryha, E. Degradation of AlSi10Mg powder during laser-based powder bed fusion processing. *Mater. Des.* **2021**, *198*, 109358. [CrossRef]
46. Min, S.; Zhang, H.; Liu, H.; Zhang, K.; Huang, A.; Hou, J. Influence of defects on high-temperature oxidation performance of GH3536 superalloys fabricated by laser powder bed fusion. *Addit. Manuf. Lett.* **2022**, *3*, 100064. [CrossRef]
47. Liang, X.; Hor, A.; Robert, C.; Salem, M.; Lin, F.; Morel, F. High cycle fatigue behavior of 316L steel fabricated by laser powder bed fusion: Effects of surface defect and loading mode. *Int. J. Fatigue* **2022**, *160*, 106843. [CrossRef]
48. Mussatto, A.; Groarke, R.; Vijayaraghavan, R.K.; Obeidi, M.A.; MacLoughlin, R.; McNally, P.J.; Nicolosi, V.; Delaure, Y.; Brabazon, D. Laser-powder bed fusion in-process dispersion of reinforcing ceramic nanoparticles onto powder beds via colloid nebulization. *Mater. Chem. Phys.* **2022**, *287*, 126245. [CrossRef]
49. Obeidi, M.A.; Conway, A.; Mussatto, A.; Dogu, M.N.; Sreenilayam, S.P.; Ayub, H.; Ahad, I.U.; Brabazon, D. Effects of powder compression and laser re-melting on the microstructure and mechanical properties of additively manufactured parts in laser-powder bed fusion. *Results Mater.* **2022**, *13*, 100264. [CrossRef]
50. Rivolta, B.; Gerosa, R.; Panzeri, D. Selective laser melted 316L stainless steel: Influence of surface and inner defects on fatigue behavior. *Int. J. Fatigue* **2023**, *172*, 107664. [CrossRef]
51. Ghosh, A.; Wang, X.; Kietzig, A.-M.; Brochu, M. Layer-by-layer combination of laser powder bed fusion (LPBF) and femtosecond laser surface machining of fabricated stainless-steel components. *J. Manuf. Process.* **2018**, *35*, 327–336. [CrossRef]
52. Chen, H.Y.; Gu, D.D.; Ge, Q.; Shi, X.Y.; Zhang, H.M.; Wang, R.; Zhang, H.; Kosiba, K. Role of laser scan strategies in defect control, microstructural evolution and mechanical properties of steel matrix composites prepared by laser additive manufacturing. *Int. J. Miner. Metall. Mater.* **2021**, *28*, 462–474. [CrossRef]
53. Javidi, M.J.; Hosseini, S.M.; Khodabakhshi, F.; Mohammadi, M.; Orovcik, L.; Trembošová, V.N.; Nagy, Š.; Nosko, M. Laser powder bed fusion of 316L stainless steel/Al2O3 nanocomposites: Taguchi analysis and material characterization. *Opt. Laser Technol.* **2023**, *158 Part A*, 108883. [CrossRef]
54. Liu, Q.; Wang, G.; Qiu, C. On the Role of Dynamic Grain Movement in Deformation and Mechanical Anisotropy Development in a Selectively Laser Melted Stainless Steel. *Addit. Manuf.* **2020**, *35*, 101329. [CrossRef]

55. Dehgahi, S.; Pirgazi, H.; Sanjari, M.; Seraj, P.; Odeshi, A.; Kestens, L.A.I.; Mohammadi, M. Effect of building direction on high strain-rate compressive behavior of heat-treated LPBF-maraging steels using Split Hopkinson pressure bar apparatus. *Mater. Sci. Eng. A* **2022**, *835*, 142653. [CrossRef]
56. Haghdadi, N.; Chen, H.; Chen, Z.; Babu, S.S.; Liao, X.; Ringer, S.P.; Primig, S. Intergranular precipitation and chemical fluctuations in an additively manufactured 2205 duplex stainless steel. *Scr. Mater.* **2022**, *219*, 114894. [CrossRef]
57. Barroux, A.; Duguet, T.; Ducommun, N.; Nivet, E.; Delgado, J.; Laffont, L.; Blanc, C. Combined XPS/TEM study of the chemical composition and structure of the passive film formed on additive manufactured 17-4PH stainless steel. *Surf. Interfaces* **2021**, *22*, 100874. [CrossRef]
58. Shakerin, S.; Hadadzadeh, A.; Amirkhiz, B.S.; Shamsdini, S.; Li, J.; Mohammadi, M. Additive manufacturing of maraging steel-H13 bimetals using laser powder bed fusion technique. *Addit. Manuf.* **2019**, *29*, 100797. [CrossRef]
59. Shen, L.C.; Yang, X.H.; Ho, J.R.; Tung, P.C.; Lin, C.K. Effects of build direction on the mechanical properties of a martensitic stainless steel fabricated by selective laser melting. *Materials* **2020**, *13*, 5142. [CrossRef] [PubMed]
60. Wan, H.Y.; Zhou, Z.J.; Li, C.P.; Chen, G.F.; Zhang, G.P. Effect of scanning strategy on mechanical properties of selective laser melted Inconel 718. *Mater. Sci. Eng.* **2019**, *753*, 42–48. [CrossRef]
61. Chen, G.; Liu, S.; Huang, C.; Ma, Y.; Li, Y.; Zhang, B.; Gao, L.; Zhang, B.; Wang, P.; Qu, X. In-situ phase transformation and corrosion behavior of TiNi via LPBF. *Corros. Sci.* **2022**, *203*, 110348. [CrossRef]
62. Guo, W.; Feng, B.; Yang, Y.; Ren, Y.; Liu, Y.; Yang, H.; Yang, Q.; Cui, L.; Tong, X.; Hao, S. Effect of laser scanning speed on the microstructure, phase transformation, and mechanical property of NiTi alloys fabricated by LPBF. *Mater. Des.* **2022**, *215*, 110460. [CrossRef]
63. Zhou, L.; Yuan, T.; Tang, J.; He, J.; Li, R. Mechanical and corrosion behavior of titanium alloys additively manufactured by selective laser melting A comparison between nearly β titanium, α titanium and α + β titanium. *Opt. Laser Technol.* **2019**, *119*, 105625. [CrossRef]
64. Gao, P.; Lan, X.; Yang, S.; Wang, Z.; Li, X.; Cao, L. Defect elimination and microstructure improvement of laser powder bed fusion β-solidifying γ-TiAl alloys via circular beam oscillation technology. *Mater. Sci. Eng. A* **2023**, *873*, 145019. [CrossRef]
65. Tripathy, M.; Gaskell, K.; Laureto, J.; Davami, K.; Beheshti, A. Elevated temperature fretting wear study of additively manufactured Inconel 625 superalloys. *Addit. Manuf.* **2023**, *67*, 103492. [CrossRef]
66. Schwerz, C.; Bircher, B.A.; Küng, A.; Nyborg, L. In-situ detection of stochastic spatter-driven lack of fusion: Application of optical tomography and validation via ex-situ X-ray computed tomography. *Addit. Manuf.* **2023**, *72*, 103631. [CrossRef]
67. Li, H.; Brodie, E.G.; Hutchinson, C. Predicting the chemical homogeneity in laser powder bed fusion (LPBF) of mixed powders after remelting. *Addit. Manuf.* **2023**, *65*, 103447. [CrossRef]
68. Pant, P.; Salvemini, F.; Proper, S.; Luzin, V.; Simonsson, K.; Sjöström, S.; Hosseini, S.; Peng, R.L.; Moverare, J. A study of the influence of novel scan strategies on residual stress and microstructure of L-shaped LPBF IN718 samples. *Mater. Des.* **2022**, *214*, 110386. [CrossRef]
69. Zhang, H.; Lu, J.; Xu, G.; Luo, K.; Okulov, I.; Xue, W. Island scan length effect on processability, microstructure, and mechanical property of laser powder bed fusion processed nickel matrix composites. *Mater. Sci. Eng. A* **2023**, *864*, 144559. [CrossRef]
70. Sanchez, S.; Hyde, C.J.; Ashcroft, I.A.; Ravi, G.A.; Clare, A.T. Multi-laser scan strategies for enhancing creep performance in LPBF. *Addit. Manuf.* **2021**, *41*, 101948. [CrossRef]
71. Sanchez, S.; Gaspard, G.; Hyde, C.J.; Ashcroft, I.A.; Ravi, G.A.; Clare, A.T. On the thermomechanical aging of LPBF alloy 718. *Mater. Sci. Eng. A* **2022**, *841*, 142998. [CrossRef]
72. Adegoke, O.; Kumara, C.; Thuvander, M.; Deirmina, F.; Andersson, J.; Brodin, H.; Harlin, P.; Pederson, R. Scanning electron microscopy and atom probe tomography characterization of laser powder bed fusion precipitation strengthening nickel-based superalloy. *Micron* **2023**, *171*, 103472. [CrossRef]
73. Kimura, T.; Nakamoto, T. Microstructures and mechanical properties of A356 (AlSi7Mg0.3) aluminum alloy fabricated by selective laser melting. *Mater. Des.* **2016**, *89*, 1294–1301. [CrossRef]
74. Kumar, M.; Gibbons, G.J.; Das, A.; Manna, I.; Tanner, D.; Kotadia, H.R. Additive manufacturing of aluminum alloy 2024 by laser powder bed fusion: Microstructural evolution, defects, and mechanical properties. *Rapid Prototyp. J.* **2021**, *27*, 1388–1397. [CrossRef]
75. Vikram, R.J.; Gokulnath, S.A.; Prashanth, K.G.; Suwas, S. Effect of scanning strategy on microstructure and texture evolution in a selective laser melted Al-33Cu eutectic alloy. *J. Alloys Compd.* **2023**, *936*, 168098. [CrossRef]
76. Nugraha, A.D.; Ruli; Supriyanto, E.; Rasgianti; Prawara, B.; Martides, E.; Junianto, E.; Wibowo, A.; Sentanuhady, J.; Muflikhun, M.A. First-rate manufacturing process of primary air fan (PAF) coal power plant in Indonesia using laser powder bed fusion (LPBF) technology. *J. Mater. Res. Technol.* **2022**, *18*, 4075–4088. [CrossRef]
77. Liu, M.; Wei, K.; Zeng, X. High power laser powder bed fusion of AlSi10Mg alloy: Effect of layer thickness on defect, microstructure, and mechanical property. *Mater. Sci. Eng. A* **2022**, *842*, 143107. [CrossRef]
78. Qin, H.; Fallah, V.; Dong, Q.; Brochu, M.; Daymond, M.R.; Gallerneault, M. Solidification pattern, microstructure, and texture development in Laser Powder Bed Fusion (LPBF) of Al10SiMg alloy. *Mater. Charact.* **2018**, *145*, 29–38. [CrossRef]
79. Wang, T.; Yang, X.; Wang, Y.; Zhu, H. Effect of 0.5 wt% Zr on defects, microstructure, and mechanical properties of Al-3.6Zn-0.6Mg alloy fabricated by laser powder bed fusion. *Metals* **2022**, *156*, 108612. [CrossRef]
80. Griffiths, S.; Rossell, M.D.; Croteau, J.; Vo, N.Q.; Dunand, D.C.; Leinenbach, C. Effect of laser rescanning on the grain microstructure of a selective laser melted Al-Mg-Zr alloy. *Mater. Charact.* **2018**, *143*, 34–42. [CrossRef]
81. Snopinski, P.; Matus, K.; Hilšer, O.; Rusz, S. Effects of Built Direction and Deformation Temperature on the Grain Refinement of 3D Printed AlSi10Mg Alloy Processed by Equal Channel Angular Pressing (ECAP). *Materials* **2023**, *16*, 4288. [CrossRef]

82. Aliyu, A.A.A.; Poungsiri, K.; Shinjo, J.; Panwisawas, C.; Reed, R.C.; Puncreobutr, C.; Tumkanon, K.; Kuimalee, S.; Lohwongwatana, B. Additive manufacturing of tantalum scaffolds: Processing, microstructure, and process-induced defects. *Int. J. Refract. Met. Hard Mater.* **2023**, *112*, 106132. [CrossRef]
83. Guaglione, F.; Caprio, L.; Previtali, B.; Demir, A.G. Single point exposure LPBF for the production of biodegradable Zn-alloy lattice structures. *Addit. Manuf.* **2021**, *48 Part A*, 102426. [CrossRef]
84. Liu, M.; Zhang, J.; Chen, C.; Geng, Z.; Wu, Y.; Li, D.; Zhang, T.; Guo, Y. Additive manufacturing of pure niobium by laser powder bed fusion: Microstructure, mechanical behavior and oxygen assisted embrittlement. *Mater. Sci. Eng. A* **2023**, *866*, 144691. [CrossRef]
85. Robinson, J.; Stanford, M.; Arjunan, A. Correlation between selective laser melting parameters, pore defects and tensile properties of 99.9% silver. *Mater. Today Commun.* **2020**, *25*, 101550. [CrossRef]
86. Zhang, J.; Gu, D.; Yang, Y.; Zhang, H.; Chen, H.; Dai, D.; Lin, K. Influence of particle size on laser absorption and scanning track formation mechanisms of pure tungsten powder during selective laser melting. *Engineering* **2019**, *5*, 736–745. [CrossRef]
87. Withers, P.J.; Bouman, C.; Carmignato, S.; Cnudde, V.; Grimaldi, D.; Hagen, C.K.; Maire, E.; Manley, M.; Plessis, A.D.; Stock, S.R. X-ray computed tomography. *Nat. Rev. Methods Primers* **2021**, *1*, 18. [CrossRef]
88. Montalbano, T.; Briggs, B.N.; Waterman, J.L.; Nimer, S.; Peitsch, C.; Sopcisak, J.; Trigg, D.; Storck, S. Uncovering the coupled impact of defect morphology and microstructure on the tensile behavior of ti-6Al-4V fabricated via laser powder bed fusion. *J. Mater. Process. Technol.* **2021**, *294*, 117113. [CrossRef]
89. Marattukalam, J.J.; Karlsson, D.; Pacheco, V.; Beran, P.; Wiklund, U.; Jansson, U.; Hjörvarsson, B.; Sahlberg, M. The effect of laser scanning strategies on texture, mechanical properties, and site-specific grain orientation in selective laser melted 316L SS. *Mater. Des.* **2020**, *193*, 108852. [CrossRef]
90. Mussatto, A.; Groarke, R.; Vijayaraghavan, R.K.; Hughes, C.; Obeidi, M.A.; Doğu, M.N.; Yalçin, M.A.; McNally, P.J.; Delaure, Y.; Brabazon, D. Assessing dependency of part properties on the printing location in laser-powder bed fusion metal additive manufacturing. *Mater. Today Commun.* **2022**, *30*, 103209. [CrossRef]
91. Cabrini, M.; Carrozza, A.; Lorenzi, S.; Pastore, T.; Testa, C.; Manfredi, D.; Fino, P.; Scenini, F. Influence of surface finishing and heat treatments on the corrosion resistance of LPBF-produced Ti-6Al-4V alloy for biomedical applications. *J. Mater. Process. Technol.* **2022**, *308*, 117730. [CrossRef]
92. Lamb, K.; Koube, K.; Kacher, J.; Sloop, T.; Thadhani, N.; Babu, S.S. Anisotropic spall failure of additively manufactured 316L stainless steel. *Addit. Manuf.* **2023**, *66*, 103464. [CrossRef]
93. Jiang, M.G.; Chen, Z.W.; Tong, J.D.; Liu, C.Y.; Xu, G.; Liao, H.B.; Wang, P.; Wang, X.Y.; Xu, M.; Lao, C.S. Strong and ductile reduced activation ferritic/martensitic steel additively manufactured by selective laser melting. *Mater. Res. Lett.* **2019**, *7*, 426–432. [CrossRef]
94. Mutua, J.; Nakata, S.; Onda, T.; Chen, Z.C. Optimization of selective laser melting parameters and influence of post heat treatment on microstructure and mechanical properties of maraging steel. *Mater. Des.* **2018**, *139*, 486–497. [CrossRef]
95. Mussatto, A.; Groarke, R.; Vijayaraghavan, R.K.; Obeidi, M.A.; McNally, P.J.; Nicolisi, V. Laser-powder bed fusion of silicon carbide reinforced 316L stainless steel using a sinusoidal laser scanning strategy. *J. Mater. Res. Technol.* **2022**, *18*, 2672–2698. [CrossRef]
96. Yang, Y.; Zeng, W.H.; Gong, X.Z.; Niu, L.H.; Wang, Y.H.; Li, S.; Xu, X.; Wang, C.Y.; Zhang, L.C. Interplay between hierarchical microstructure and graded residual stress in a stainless steel fabricated by laser powder bed fusion. *Mater. Charact.* **2023**, *200*, 112912. [CrossRef]
97. Gainov, R.R.; Faidel, D.; Behr, W.; Natour, G.; Pauly, F.; Willms, H.; Vagizov, F.G. Investigation of LPBF A800H steel parts using Computed Tomography and Mössbauer spectroscopy. *Addit. Manuf.* **2020**, *32*, 101035. [CrossRef]
98. Forien, J.-B.; Calta, N.P.; DePond, P.J.; Guss, G.M.; Roehling, T.T.; Matthews, M.J. Detecting keyhole pore defects and monitoring process signatures during laser powder bed fusion: A correlation between in situ pyrometry and ex-situ X-ray radiography. *Addit. Manuf.* **2020**, *35*, 101336. [CrossRef]
99. Guerra, M.G.; Lafirenza, M.; Errico, V.; Angelastro, A. In-process dimensional and geometrical characterization of laser-powder bed fusion lattice structures through high-resolution optical tomography. *Opt. Laser Technol.* **2023**, *162*, 109252. [CrossRef]
100. Puttonen, T.; Chekurov, S.; Kuva, J.; Björkstrand, R.; Partanen, J.; Salmi, M. Influence of feature size and shape on corrosion of 316L lattice structures fabricated by laser powder bed fusion. *Addit. Manuf.* **2023**, *61*, 103288. [CrossRef]
101. Attar, H.; Prashanth, K.G.; Zhang, L.-C.; Calin, M.; Okulov, I.V.; Scudino, S.; Yang, C.; Eckert, J. Effect of Powder Particle Shape on the Properties of In Situ Ti-TiB Composite Materials Produced by Selective Laser Melting. *J. Mater. Sci. Technol.* **2015**, *31*, 1001–1005. [CrossRef]
102. Attar, H.; Löber, L.; Funk, A.; Calin, M.; Zhang, L.; Prashanth, K.; Scudino, S.; Zhang, Y.; Eckert, J. Mechanical behavior of porous commercially pure Ti and Ti-TiB composite materials manufactured by selective laser melting. *Mater. Sci. Eng. A* **2015**, *625*, 350–356. [CrossRef]
103. Baldin, E.K.; Castro, V.V.d.; Santos, P.B.; Aguzzoli, C.; Bernardi, F.; Medeiros, T.; Maurmann, N.; Pranke, P.; Frassini, R.; Roesh, M.E.; et al. Copper incorporation by low-energy ion implantation in PEO-coated additively manufactured Ti6Al4V ELI: Surface microstructure, cytotoxicity and antibacterial behavior. *J. Alloys Compd.* **2023**, *940*, 168735. [CrossRef]
104. Promoppatum, P.; Chayasombat, B.; Soe, A.; Sombatmai, A.; Sato, Y.; Suga, T.; Tsukamoto, M. In-situ modification of thermal, microstructural, and mechanical responses by altering scan lengths in laser powder bed fusion additive manufacturing of Ti-6Al-4V. *Opt. Laser Technol.* **2023**, *164*, 109525. [CrossRef]
105. Gray, J.; Depcik, C.; Sietins, J.M.; Kudzal, A.; Rogers, R.; Cho, K. Production of the cylinder head and crankcase of a small internal combustion engine using metal laser powder bed fusion. *J. Manuf. Process.* **2023**, *97*, 100–114. [CrossRef]

106. Marcu, T.; Todea, M.; Maines, L.; Leordean, D.; Berce, P.; Popa, C. Metallurgical and mechanical characterization of titanium-based materials for endosseous applications obtained by selective laser melting. *Powder Metall.* **2012**, *55*, 309–314. [CrossRef]
107. Meng, L.X.; Ben, D.D.; Yang, H.J.; Ji, H.B.; Lian, D.L.; Zhu, Y.K.; Chen, J.; Yi, J.L.; Wang, L.; Yang, J.B.; et al. Effects of embedded spherical pore on the tensile properties of a selective laser melted Ti6Al4V alloy. *Mater. Sci. Eng.* **2021**, *815*, 141254. [CrossRef]
108. Zhou, X.; Dai, N.; Chu, M.; Wang, L.; Li, D.; Zhou, L.; Cheng, X. X-ray CT analysis of the influence of process on defect in Ti-6Al-4V parts produced with Selective Laser Melting technology. *Int. J. Adv. Manuf. Technol.* **2020**, *106*, 3–14. [CrossRef]
109. Parizia, S.; Marchese, G.; Rashidi, M.; Lorusso, M.; Hryha, E.; Manfredi, D.; Biamino, S. Effect of heat treatment on microstructure and oxidation properties of Inconel 625 processed by LPBF. *J. Alloys Compd.* **2020**, *846*, 156418. [CrossRef]
110. Mirkoohi, E.; Liang, S.Y.; Tran, H.C.; Lo, Y.L.; Chang, Y.C.; Lin, H.Y. Mechanics modeling of residual stress considering effect of preheating in laser powder bed fusion. *J. Manuf. Mater. Process.* **2021**, *5*, 46. [CrossRef]
111. Song, X.; Feih, S.; Zhai, W.; Sun, C.-N.; Li, F.; Maiti, R.; Wei, J.; Yang, Y.; Oancea, V.; Brandt, L.R. Advances in additive manufacturing process Simulation: Residual stresses and distortion predictions in complex metallic components. *Mater. Des.* **2020**, *193*, 108779. [CrossRef]
112. Wang, Z.; Yang, Z.; Liu, F.; Zhang, W. Influence of the scanning angle on the grain growth and mechanical properties of Ni10Cr6W1Fe9Ti1 HEA fabricated using the LPBF–AM method. *Mater. Sci. Eng. A* **2023**, *864*, 144596. [CrossRef]
113. Liu, X.; Hu, R.; Zou, H.; Yang, C.; Luo, X.; Bai, J.; Ma, R. Investigation of cracking mechanism and yield strength associated with scanning strategy for an additively manufactured nickel-based superalloy. *J. Alloys Compd.* **2023**, *938*, 168532. [CrossRef]
114. Naragani, D.P.; Park, J.-S.; Kenesei, P.; Sangid, M.D. Void coalescence and ductile failure in IN718 investigated via high-energy synchrotron X-ray tomography and diffraction. *J. Mech. Phys. Solids* **2020**, *145*, 104155. [CrossRef]
115. Cordova, L.; Bor, T.; Smit, M.d.; Carmignato, S.; Campos, M.; Tinga, T. Effects of powder reuse on the microstructure and mechanical behavior of Al-Mg–Sc–Zr alloy processed by laser powder bed fusion (LPBF). *Addit. Manuf.* **2020**, *36*, 101625. [CrossRef]
116. Novak, N.; Biasetto, L.; Rebesan, P.; Zanini, F.; Carmignato, S.; Krstulović-Opara, L.; Vesenjak, M.; Ren, Z. Experimental and computational evaluation of tensile properties of additively manufactured hexa-and tetrachiral auxetic cellular structures. *Addit. Manuf.* **2021**, *45*, 102022. [CrossRef]
117. Yadav, P.; Singh, V.K.; Joffre, T.; Rigo, O.; Arvieu, C.; Guen, E.L.; Lacoste, E. Inline Drift Detection Using Monitoring Systems and Machine Learning in Selective Laser Melting. *Adv. Eng. Mater.* **2020**, *22*, 12. [CrossRef]
118. Johnson, Q.C.; Laursen, C.M.; Spear, A.D.; Carroll, J.D.; Noell, P.J. Analysis of the interdependent relationship between porosity, deformation, and crack growth during compression loading of LPBF AlSi10Mg. *Mater. Sci. Eng. A* **2022**, *852*, 143640. [CrossRef]
119. Wits, W.W.; Amsterdam, E. Fatigue prediction and life assessment method for metal laser powder bed fusion parts. *CIRP Ann.* **2023**, *72*, 129–132. [CrossRef]
120. Chen, H.; Patel, S.; Vlasea, M.; Zou, Y. Enhanced tensile ductility of an additively manufactured AlSi10Mg alloy by reducing the density of melt pool boundaries. *Scr. Mater.* **2022**, *221*, 114954. [CrossRef]
121. Atapour, M.; Sanaei, S.; Wei, Z.; Sheikholeslam, M.; Henderson, J.D.; Eduok, U.; Hosein, Y.K.; Holdsworth, D.W.; Hedberg, Y.S.; Ghorbani, H.R. In vitro corrosion and biocompatibility behavior of CoCrMo alloy manufactured by laser powder bed fusion parallel and perpendicular to the build direction. *Electrochim. Acta* **2023**, *445*, 142059. [CrossRef]
122. Zhang, S.; Zhu, H.; Hu, Z.; Zeng, X.; Zhong, F. Selective Laser Melting of Cu10Zn alloy powder using high laser power. *Powder Technol.* **2019**, *342*, 613–620. [CrossRef]
123. Kim, F.H.; Moylan, S.P.; Garboczi, E.J.; Slotwinski, J.A. Investigation of pore structure in cobalt chrome additively manufactured parts using X-ray computed tomography and three-dimensional image analysis. *Addit. Manuf.* **2017**, *17*, 23–38. [CrossRef]
124. Cao, L.; Li, J.; Hu, J.; Liu, H.; Wu, Y.; Zhou, Q. Optimization of surface roughness and dimensional accuracy in LPBF additive manufacturing. *Opt. Laser Technol.* **2021**, *142*, 107246. [CrossRef]
125. Grasso, M.; Laguzza, V.; Semeraro, Q.; Colosimo, B.M. In-process monitoring of selective laser melting: Spatial detection of defects via image data analysis. *J. Manuf. Sci. Eng.* **2017**, *139*, 051001. [CrossRef]
126. Dolan, E.B.; Verbruggen, S.W.; Rolfe, R.A. Chapter 1–Techniques for studying mechanobiology. In *Mechanobiology in Health and Disease*; Academic Press: Cambridge, MA, USA, 2018; pp. 1–53. [CrossRef]
127. Sun, Z.; Chueh, Y.H.; Li, L. Multiphase mesoscopic Simulation of multiple and functionally gradient materials laser powder bed fusion additive manufacturing processes. *Addit. Manuf.* **2020**, *35*, 101448. [CrossRef]
128. Köhler, M.L.; Kunz, J.; Herzog, S.; Kaletsch, A.; Broeckmann, C. Microstructure analysis of novel LPBF-processed duplex stainless steels correlated to their mechanical and corrosion properties. *Mater. Sci. Eng. A* **2021**, *801*, 140432. [CrossRef]
129. Alfieri, V.; Giannella, V.; Caiazzo, F.; Sepe, R. Influence of position and building orientation on the static properties of LPBF specimens in 17-4 PH stainless steel. *Forces Mech.* **2022**, *8*, 100108. [CrossRef]
130. Wang, P.; Lei, H.; Zhu, X.; Chen, H.-C.; Fang, D. Influence of manufacturing geometric defects on the mechanical properties of AlSi10Mg alloy fabricated by selective laser melting. *J. Alloys Compd.* **2019**, *789*, 852–859. [CrossRef]
131. Liu, C.Y.; Tong, J.D.; Jiang, M.G.; Chen, Z.W.; Xu, G.; Liao, H.B.; Wang, P.; Wang, X.Y.; Xu, M.; Lao, C.S. Effect of scanning strategy on microstructure and mechanical properties of selective laser melted reduced activation ferritic/martensitic steel. *Mater. Sci. Eng.* **2019**, *766*, 138364. [CrossRef]
132. Nie, J.; Wei, L.; Li, D.-l.; Zhao, L.; Jiang, Y.; Li, Q. High-throughput characterization of microstructure and corrosion behavior of additively manufactured SS316L-SS431graded material. *Addit. Manuf.* **2020**, *35*, 101295. [CrossRef]

133. Gobert, C.; Reutzel, E.W.; Petrich, J.; Nassar, A.R.; Phoha, S. Application of supervised machine learning for defect detection during metallic powder bed fusion additive manufacturing using high-resolution imaging. *Addit. Manuf.* **2018**, *21*, 517–528. [CrossRef]
134. Bonatti, C.; Mohr, D. Mechanical performance of additively manufactured anisotropic and isotropic smooth shell-lattice materials: Simulations & experiments. *J. Mech. Phys. Solids* **2019**, *122*, 1–26. [CrossRef]
135. Wilson-Heid, A.E.; Qin, S.; Beese, A.M. Multiaxial plasticity and fracture behavior of stainless steel 316L by laser powder bed fusion: Experiments and computational modeling. *Acta Mater.* **2020**, *199*, 578–592. [CrossRef]
136. Wilson-Heid, A.E.; Beese, A.M. Combined effects of porosity and stress state on the failure behavior of laser powder bed fusion stainless steel 316L. *Addit. Manuf.* **2021**, *39*, 101862. [CrossRef]
137. Jin, P.; Tang, Q.; Song, J.; Feng, Q.; Guo, F.; Fan, X.; Jin, M.; Wang, F. Numerical investigation of the mechanism of interfacial dynamics of the melt pool and defects during laser powder bed fusion. *Opt. Laser Technol.* **2021**, *143*, 107289. [CrossRef]
138. Mishra, A.K.; Kumar, A. Govind, Development and validation of a material evaporation assisted thermal model for time-efficient calculation of thermal and solidification parameters during laser powder bed fusion process for Ti6Al4V. *Addit. Manuf.* **2023**, *66*, 103453. [CrossRef]
139. Mishurova, T.; Artzt, K.; Rehmer, B.; Haubrich, J.; Ávila, L.; Schoenstein, F.; Serrano-Munoz, I.; Requena, G.; Bruno, G. Separation of the impact of residual stress and microstructure on the fatigue performance of LPBF Ti-6Al-4V at elevated temperature. *Int. J. Fatigue* **2021**, *148*, 106239. [CrossRef]
140. Attar, H.; Ehtemam-Haghighi, S.; Kent, D.; Wu, X.; Dargusch, M.S. Comparative study of commercially pure titanium produced by laser engineered net shaping, selective laser melting and casting processes. *Mater. Sci. Eng. A* **2017**, *705*, 385–393. [CrossRef]
141. Attar, H.; Bermingham, M.; Ehtemam-Haghighi, S.; Dehghan-Manshadi, A.; Kent, D.; Dargusch, M. Evaluation of the mechanical and wear properties of titanium produced by three different additive manufacturing methods for biomedical application. *Mater. Sci. Eng. A* **2019**, *760*, 339–345. [CrossRef]
142. Liu, F.; Chen, Y.; Li, L.; Wang, C.; Wang, Q.; Liu, Y. Interior defect-induced crack initiation mechanism and initial growth behavior for Ti6Al4V alloy fabricated using laser powder bed fusion. *J. Mater. Res. Technol.* **2022**, *21*, 2089–2104. [CrossRef]
143. Alghamdi, A.; Maconachie, T.; Downing, D.; Brandt, M.; Qian, M.; Leary, M. Effect of additive manufactured lattice defects on mechanical properties: An automated method for the enhancement of lattice geometry. *Int. J. Adv. Manuf. Technol.* **2020**, *108*, 957–971. [CrossRef]
144. Becker, T.; Altenburg, S.J.; Scheuschner, N.; Bresse, P.P.; Metz, C.; Hilgenberg, K.; Maierhofer, C. In-situ monitoring of the Laser Powder Bed Fusion build process via bi-chromatic optical tomography. *Procedia CIRP* **2022**, *111*, 340–344. [CrossRef]
145. Singh, A.; Caprio, L.; Previtali, B.; Demir, A.G. Processability of pure Cu by LPBF using a ns-pulsed green fiber laser. *Opt. Laser Technol.* **2022**, *154*, 108310. [CrossRef]
146. Lodhi, M.J.K.; Deen, K.M.; Greenlee-Wacker, M.C.; Haider, W. Additively manufactured 316L stainless steel with improved corrosion resistance and biological response for biomedical applications. *Addit. Manuf.* **2019**, *27*, 8–19. [CrossRef]
147. Cheng, Q.; Zhuang, X. Quasi-in-situ monitoring of passive film growth of Inconel 718 alloy. *Mater. Lett.* **2023**, *335*, 133743. [CrossRef]
148. Montazeri, M.; Nassar, A.R.; Dunbar, A.J.; Rao, P. In-process monitoring of porosity in additive manufacturing using optical emission spectroscopy. *IISE Trans.* **2019**, *52*, 500–515. [CrossRef]
149. Hooper, P.A. Melt pool temperature and cooling rates in laser powder bed fusion. *Addit. Manuf.* **2018**, *22*, 548–559. [CrossRef]
150. Santospirito, S.P.; Laptka, R.; Cerniglia, D.; Slyk, K.; Luo, B.; Panggabean, D.; Rudlin, J. Defect detection in laser powder deposition components by laser thermography and laser ultrasonic inspections. In *Frontiers in Ultrafast Optics: Biomedical, Scientific, and Industrial Applications XIII*; SPIE: San Diego, CA, USA, 2013; p. 8611. [CrossRef]
151. Clijsters, S.; Craeghs, T.; Buls, S.; Kempen, K.; Kruth, J.-P. In situ quality control of the selective laser melting process using a high-speed, real-time melt pool monitoring system. *Int. J. Adv. Manuf. Technol.* **2014**, *75*, 1089–1101. [CrossRef]
152. Andreyevna, D.M.; Vladimirovich, Z.I.; Ilyich, T.V.; Phillippe, B.; Yuryevich, S.I. Determination of true temperature in selective laser melting of metal powder using infrared camera. *Mater. Sci. Forum* **2015**, *834*, 93–102. [CrossRef]
153. Cerniglia, D.; Montinaro, N. Defect Detection in Additively Manufactured Components: Laser Ultrasound and Laser Thermography Comparison. *Procedia Struct. Integr.* **2018**, *8*, 154–162. [CrossRef]
154. Montinaro, N.; Cerniglia, D.; Pitarresi, G. Defect detection in additively manufactured titanium prosthesis by flying laser scanning thermography. *Procedia Struct. Integr.* **2018**, *12*, 165–172. [CrossRef]
155. Wei, J.; He, Y.; Wang, F.; He, Y.; Rong, X.; Chen, M.; Wang, Y.; Yue, H.; Liu, J. Convolutional neural network assisted infrared imaging technology: An enhanced online processing state monitoring method for laser powder bed fusion. *Infrar. Phys. Technol.* **2023**, *131*, 104661. [CrossRef]
156. Lough, C.S.; Wang, X.; Smith, C.C.; Landers, R.G.; Bristow, D.A.; Drallmeier, J.A.; Brown, B.; Kinzel, E.C. Correlation of SWIR imaging with LPBF 304L stainless steel part properties. *Addit. Manuf.* **2020**, *35*, 101359. [CrossRef]
157. Estalaki, S.M.; Lough, C.S.; Landers, R.G.; Kinzel, E.C.; Luo, T. Predicting defects in laser powder bed fusion using in-situ thermal imaging data and machine learning. *Addit. Manuf.* **2022**, *58*, 103008. [CrossRef]
158. Vallabh, C.K.P.; Zhao, X. Melt pool temperature measurement and monitoring during laser powder bed fusion based additive manufacturing via single-camera two-wavelength imaging pyrometry (STWIP). *J. Manuf. Process.* **2022**, *79*, 486–500. [CrossRef]
159. Vallabh, C.K.P.; Sridar, S.; Xiong, W.; Zhao, X. Predicting melt pool depth and grain length using multiple signatures from in-situ single camera two-wavelength imaging pyrometry for laser powder bed fusion. *J. Mater. Process. Technol.* **2022**, *308*, 117724. [CrossRef]
160. Zhang, H.; Vallabh, C.K.P.; Zhao, X. Registration and fusion of large-scale melt pool temperature and morphology monitoring data demonstrated for surface topography prediction in LPBF. *Addit. Manuf.* **2022**, *58*, 103075. [CrossRef]

161. Forien, J.-B.; Guss, G.; Khairallah, S.; Smith, W.; DePond, P.; Matthews, M.; Calta, N. Detecting missing struts in metallic micro-lattices using high-speed melt pool thermal monitoring. *Addit. Manuf. Lett.* **2023**, *4*, 100112. [CrossRef]
162. Duong, E.; Masseling, L.; Knaak, C.; Dionne, P.; Megahed, M. Scan path resolved thermal modeling of LPBF. *Addit. Manuf. Lett.* **2022**, *3*, 100047. [CrossRef]
163. Kozjek, D.; Porter, C.; Carter, F.M., III; Mogonye, J.-E.; Cao, J. Data-driven prediction of geometry- and toolpath sequence-dependent intra-layer process conditions variations in laser powder bed fusion. *J. Manuf. Process.* **2023**, *100*, 34–46. [CrossRef]
164. Boettinger, W.J.; Kattner, U.R.; Moon, K.-W.; Perepezko, J.H. Chapter Five-DTA and Heat-flux DSC Measurements of Alloy Melting and Freezing. In *Methods for Phase Diagram Determination*; Elsevier: Amsterdam, The Netherlands, 2007; pp. 151–221. [CrossRef]
165. Zhuravlev, E.; Milkereit, B.; Yang, B.; Heiland, S.; Vieth, P.; Voigt, M.; Schaper, M.; Grundmeier, G.; Schick, C.; Kessler, O. Assessment of AlZnMgCu alloy powder modification for crack-free laser powder bed fusion by differential fast scanning calorimetry. *Mater. Des.* **2021**, *204*, 109677. [CrossRef]
166. Takata, N.; Liu, M.; Li, H.; Suzuki, A.; Kobashi, M. Fast scanning calorimetry study of Al alloy powder for understanding microstructural development in laser powder bed fusion. *Mater. Des.* **2022**, *219*, 110830. [CrossRef]
167. Gholizadeh, S.; Lemana, Z.; Baharudin, B.T.H.T. A review of the application of acoustic emission technique in engineering. *Struct. Eng. Mech.* **2015**, *54*, 1075–1095. [CrossRef]
168. Strantza, M.; Ganeriwala, R.K.; Clausen, B.; Phan, T.Q.; Levine, L.E.; Pagan, D.C.; Ruff, J.P.C.; King, W.E.; Johnson, N.S.; Martinez, R.M.; et al. Effect of the scanning strategy on the formation of residual stresses in additively manufactured Ti-6Al-4V. *Addit. Manuf.* **2021**, *45*, 102003. [CrossRef]
169. Ibrahim, Y.; Li, Z.; Davies, C.M.; Maharaj, C.; Dear, J.P.; Hooper, P.A. Acoustic resonance testing of additive manufactured lattice structures. *Addit. Manuf.* **2018**, *24*, 566–576. [CrossRef]
170. Barile, C.; Casavola, C.; Pappalettera, G.; Kanna, V.P.; Renna, G. Acoustic emission signal processing for the assessment of corrosion behavior in additively manufactured AlSi10Mg. *Mech. Mater.* **2022**, *170*, 104347. [CrossRef]
171. Seleznev, M.; Gustmann, T.; Friebel, J.M.; Peuker, U.A.; Kühn, U.; Hufenbach, J.K.; Hiermann, H.; Weidner, A. In situ detection of cracks during laser powder bed fusion using acoustic emission monitoring. *Addit. Manuf. Lett.* **2022**, *3*, 100099. [CrossRef]
172. Trolinger, J.D.; Lal, A.; Dioumaev, A.; Dimas, D. A non-destructive evaluation system for additive manufacturing based on acoustic signature analysis with laser Doppler vibrometry. In *Interferometry XIX*; SPIE: San Diego, CA, USA, 2018; p. 107490. [CrossRef]
173. Ye, D.; Hong, G.S.; Zhang, Y.; Zhu, K.; Fuh, J.Y.H. Defect detection in selective laser melting technology by acoustic signals with deep belief networks. *Int. J. Adv. Manuf. Technol.* **2018**, *96*, 2791–2801. [CrossRef]
174. Drissi-Daoudi, R.; Masinelli, G.; Formanoir, C.; Wasmer, K.; Jhabvala, J.; Logé, R.E. Acoustic emission for the prediction of processing regimes in Laser Powder Bed Fusion, and the generation of processing maps. *Addit. Manuf.* **2023**, *67*, 103484. [CrossRef]
175. Kononenko, D.Y.; Nikonova, V.; Seleznev, M.; Brink, J.v.d.; Chernyavsky, D. An in-situ crack detection approach in additive manufacturing based on acoustic emission and machine learning. *Addit. Manuf. Lett.* **2023**, *5*, 100130. [CrossRef]
176. Kashyap, R. *Fiber Bragg Gratting*, 2nd ed.; Elsevier: Amsterdam, The Netherlands, 2009.
177. Jinachandran, S.; Rajan, G. Fibre Bragg Grating Based Acoustic Emission Measurement System for Structural Health Monitoring Applications. *Materials* **2021**, *14*, 897. [CrossRef]
178. Wasmer, K.; Le-Quang, T.; Meylan, B.; Shevchik, S.A. In situ Quality monitoring in AM Using Acoustic Emission: A Reinforcement Learning Approach. *J. Mater. Eng. Perform.* **2018**, *28*, 666–672. [CrossRef]
179. Shevchik, S.A.; Kenel, C.; Leinenbach, C.; Wasmer, K. Acoustic emission for in situ quality monitoring in additive manufacturing using spectral convolutional neural networks. *Addit. Manuf.* **2018**, *21*, 598–604. [CrossRef]
180. Shevchik, S.A.; Masinelli, G.; Kenel, C.; Leinenbach, C.; Wasmer, K. Deep Learning for in situ and Real-Time Quality monitoring in Additive Manufacturing Using Acoustic Emission. *IEEE Trans. Ind. Inform.* **2019**, *15*, 5194–5203. [CrossRef]
181. Johnson, W.L.; Benzing, J.T.; Kafka, O.L.; Moser, N.H.; Harris, D.; Iten, J.J.; Hrabe, N.W. Sensitivity of acoustic nonlinearity and loss to residual porosity in additively manufactured aluminum. *NDT E Int.* **2023**, *135*, 102801. [CrossRef]
182. Song, Y.; Zi, X.; Fu, Y.; Li, X.; Chen, C.; Zhou, K. Nondestructive testing of additively manufactured material based on ultrasonic scattering measurement. *Measurement* **2018**, *118*, 105–112. [CrossRef]
183. Davis, G.; Nagarajah, R.; Palanisamy, S.; Rashid, R.A.R.; Pajagopal, P.; Balasubramaniam, K. Laser ultrasonic inspection of additive manufactured components. *Int. J. Adv. Manuf. Technol.* **2019**, *102*, 2571–2579. [CrossRef]
184. Honarvar, F.; Patel, S.; Vlasea, M.; Amini, H.; Varvani-Farahani, A. Nondestructive characterization of laser powder bed fusion components using high-frequency phased array ultrasonic testing. *J. Mater. Eng. Perform.* **2021**, *30*, 6766–6776. [CrossRef]
185. Everton, S.; Dickens, P.; Tuck, C.J.; Dutton, B. *Identification of Sub-Surface Defects in Parts Produced by Additive Manufacturing, Using Laser-Generated Ultrasound*; University of Nottingham: Nottingham, UK, 2019; Available online: https://www.nottingham.ac.uk/research/groups/advanced-manufacturing-technology-research-group/documents/manufacturing-metrology-team/sarah-mst-2016.pdf (accessed on 7 July 2024).
186. Everton, S.; Dickens, P.; Tuck, C.; Dutton, B. Using laser ultrasound to detect subsurface defects in metal laser powder bed fusion components. *J. Miner.* **2018**, *70*, 378–383. [CrossRef]
187. Liu, S.; Jia, K.; Wan, H.; Ding, L.; Xu, X.; Cheng, L.; Zhang, S.; Yan, X.; Lu, M.; Ma, G.; et al. Inspection of the internal defects with different size in Ni and Ti additive manufactured components using laser ultrasonic technology. *Opt. Laser Technol.* **2022**, *146*, 107543. [CrossRef]
188. Hayashi, T.; Mori, N.; Ueno, T. Non-contact imaging of subsurface defects using a scanning laser source. *Ultrasonics* **2022**, *119*, 106560. [CrossRef]

189. Chen, Y.; Jiang, L.; Peng, Y.; Wang, M.; Xue, Z.; Wu, J.; Yang, Y.; Zhang, J. Ultra-fast laser ultrasonic imaging method for online inspection of metal additive manufacturing. *Opt. Laser Technol.* **2023**, *160*, 107244. [CrossRef]
190. Slotwinski, J.A.; Garboczi, E.J.; Hebenstreit, K.M. Porosity measurements and analysis for metal additive manufacturing process control. *J. Res. Natl. Inst. Stand. Technol.* **2014**, *119*, 494–528. [CrossRef]
191. Ladewig, A.; Schlick, G.; Fisser, M.; Schulze, V.; Glatzel, U. Influence of the shielding gas flow on the removal of process by-products in the selective laser melting process. *Addit. Manuf.* **2016**, *10*, 1–9. [CrossRef]
192. Roy, M.; Walton, K.; Harley, J.B.; Skliar, M. Ultrasonic Evaluation of Segmental Variability in Additively Manufactured Metal Components. In Proceedings of the 2018 IEEE International Ultrasonics Symposium (IUS), Kobe, Japan, 22–25 October 2018. [CrossRef]
193. Kim, C.; Yin, H.; Shmatok, A.; Prorok, B.C.; Lou, X.; Matlack, K.H. Ultrasonic nondestructive evaluation of laser powder bed fusion 316l stainless steel. *Addit. Manuf.* **2021**, *38*, 101800. [CrossRef]
194. Raffestin, M.; Domashenkov, A.; Bertrand, P.; Faverjon, P.; Courbon, C. Ultrasonic diagnostic for in situ control in metal additive manufacturing. *Measurement* **2023**, *206*, 112244. [CrossRef]
195. McGuigan, S.; Arguelles, A.P.; Obaton, A.-F.; Donmez, A.M.; Riviere, J.; Shokouhi, P. Resonant ultrasound spectroscopy for quality control of geometrically complex additively manufactured components. *Addit. Manuf.* **2021**, *39*, 101808. [CrossRef]
196. Angel, R.J.; Jackson, J.M.; Reichmann, H.J.; Speziale, S. Elasticity measurements on minerals: A review. *Eur. J. Mineral.* **2009**, *21*, 525–550. [CrossRef]
197. Garlea, E.; Choo, H.; Sluss, C.C.; Koehler, M.R.; Bridges, R.L.; Xiao, X.; Ren, Y.; Jared, B.H. Variation of elastic mechanical properties with texture, porosity, and defect characteristics in laser powder bed fusion 316L stainless steel. *Mater. Sci. Eng. A* **2019**, *763*, 138032. [CrossRef]
198. Bozek, E.; McGuigan, S.; Snow, Z.; Reutzel, E.W.; Rivière, J.; Shokouhi, P. Nonlinear resonance ultrasonic spectroscopy (NRUS) for the quality control of additively manufactured samples. *NDT E Int.* **2021**, *123*, 102495. [CrossRef]
199. Rossin, J.; Leser, P.; Pusch, K.; Frey, C.; Murray, S.P.; Torbet, C.J.; Smith, S.; Daly, S.; Pollock, T.M. Bayesian inference of elastic constants and texture coefficients in additively manufactured cobalt-nickel superalloys using resonant ultrasound spectroscopy. *Acta Mater.* **2021**, *220*, 117287. [CrossRef]
200. Bourdais, F.L.; Rathore, J.S.; Ly, C.; Pellat, M.; Vienne, C.; Bonnefoy, V.; Bergeaud, V.; Garandet, J.-P. On the potential of Resonant Ultrasound Spectroscopy applied to the non-destructive characterization of the density of (LPBF) additively manufactured materials. *Addit. Manuf.* **2022**, *58*, 103037. [CrossRef]
201. Lopez, A.B.; Santos, J.; Sousa, J.P.; Santos, T.G.; Quintino, L. Phased array ultrasonic inspection of metal additive manufacturing parts. *J. Nondestruct. Eval.* **2019**, *38*, 62. [CrossRef]
202. Allam, A.; Alfahmi, O.; Sugino, C.; Harding, M.; Ruzzene, M.; Erturk, A. Ultrasonic testing of thick and thin Inconel 625 alloys manufactured by laser powder bed fusion. *Ultrasonics* **2022**, *125*, 106780. [CrossRef]
203. Stratoudaki, T.; Javadi, Y.; Kerr, W.; Wilcox, P. Laser induced phased arrays for remote ultrasonic imaging of additive manufactured components. In Proceedings of the 57th Annual Conference of the British Institute of Non-Destructive Testing, Nottingham, UK, 10–12 September 2018.
204. Du, W.; Bai, Q.; Wang, Y.; Zhang, B. Eddy current detection of subsurface defects for additive/subtractive hybrid manufacturing. *Int. J. Adv. Manuf. Technol.* **2018**, *95*, 3185–3195. [CrossRef]
205. Goodall, A.D.; Yiannakou, G.; Chechik, L.; Mitchell, R.L.; Jewell, G.W.; Todd, I. Geometrical control of eddy currents in additively manufactured Fe-Si. *Mater. Des.* **2023**, *230*, 112002. [CrossRef]
206. Smith, W.L.; Roehling, J.D.; Strantza, M.; Ganeriwala, R.K.; Ashby, A.S.; Vrancken, B.; Clausen, B.; Guss, G.M.; Brown, D.W.; McKeown, J.T.; et al. Residual stress analysis of in situ surface layer heating effects on laser powder bed fusion of 316L stainless steel. *Addit. Manuf.* **2021**, *47*, 102252. [CrossRef]
207. Zadeh, M.K.; Yeganeh, M.; Shoushtari, M.T.; Ramezanalizadeh, H.; Seidi, F. Microstructure, corrosion behavior, and biocompatibility of Ti-6Al-4 V alloy fabricated by LPBF and EBM techniques. *Mater. Today Commun.* **2022**, *31*, 103502. [CrossRef]
208. Ghosh, A.; Kumar, A.; Wang, X.; Kietzig, A.-M.; Brochu, M. Analysis of the effect of surface morphology on tensile behavior of LPBF SS316L microstruts. *Mater. Sci. Eng. A* **2022**, *831*, 142226. [CrossRef]
209. Ewald, F.C.; Brenne, F.; Gustmann, T.; Vollmer, M.; Krooß, P.; Niendorf, T. Laser Powder Bed Fusion Processing of Fe-Mn-Al-Ni Shape Memory Alloy—On the Effect of Elevated Platform Temperatures. *Metals* **2021**, *11*, 185. [CrossRef]
210. Jiang, C.-P.; Maidhah, A.A.; Wang, S.-H.; Wang, Y.-R.; Pasang, T.; Ramezani, M. Laser Powder Bed Fusion of Inconel 718 Tools for Cold Deep Drawing Applications: Optimization of Printing and Post-Processing Parameters. *Materials* **2023**, *16*, 4707. [CrossRef]
211. Sprouster, D.J.; Cunningham, W.S.; Halada, G.P.; Yan, H.; Pattammattel, A.; Huang, X.; Olds, D.; Tilton, M.; Chu, Y.S.; Dooryhee, E.; et al. Dislocation microstructure and its influence on corrosion behavior in laser additively manufactured 316L stainless steel. *Addit. Manuf.* **2021**, *47*, 102263. [CrossRef]
212. Heifetz, A.; Zhang, X.; Saniie, J.; Cleary, W. *Detection of Defects in Additively Manufactured Metallic Materials with Machine Learning of Pulsed Thermography Images*; Argonne National Laboratory: Argonne, IL, USA; Illinois Institute of Technology: Chicago, IL, USA; Westinghouse Electric Company: Columbia, SC, USA, 2020; ANL-20/57.
213. Simmons, J.C.; Chen, X.; Azizi, A.; Daeumer, M.A.; Zavalij, P.Y.; Zhou, G.; Schiffres, S.N. Influence of processing and microstructure on the local and bulk thermal conductivity of selective laser melted 316L stainless steel. *Addit. Manuf.* **2020**, *32*, 100996. [CrossRef]
214. Yang, X.; Yagodzinskyy, Y.; Ge, Y.; Lu, E.; Lehtonen, J.; Kollo, L.; Hannula, S.-P. Hydrogen Effects in Equiatomic CrFeNiMn Alloy Fabricated by Laser Powder Bed Fusion. *Metals* **2021**, *11*, 872. [CrossRef]

215. Ramakrishnan, T.; Kumar, A.; Kumar, T.S.; Kwon, S.; Muniz-Lerma, J.A.; Gauvin, R.; Brochu, M. Crack-Free Tungsten Fabricated via Laser Powder Bed Fusion Additive Manufacturing. *Adv. Func. Mater.* **2023**, *34*, 2309304. [CrossRef]
216. Smith, R.J.; Hirsch, M.; Patel, R.; Li, W.; Clare, A.T.; Sharples, S.D. Spatially resolved acoustic spectroscopy for selective laser melting. *J. Mater. Process. Technol.* **2016**, *236*, 93–102. [CrossRef]
217. Shishkovsky, I.V.; Sheng, B.; Kanfoud, J.; Gan, T.-H. *Advanced Additive Manufacturing-Ch 8: Quality Control of Metal Additive Manufacturing*; IntechOpen: London, UK, 2022. [CrossRef]
218. Liu, Y.; Wang, X.; Oliveira, J.P.; He, J.; Guan, X. Spatial and directional characterization of wire and arc additive manufactured aluminum alloy using phased array ultrasonic backscattering method. *Ultrasonic* **2023**, *132*, 107024. [CrossRef]
219. Cui, Y.; Chen, L.; Wang, L.; Cheng, J.; Zhang, L. Response of the Metastable Pitting Corrosion of Laser Powder Bed Fusion Produced Ti–6Al–4V to H+ Concentration Changes. *Metals* **2023**, *13*, 514. [CrossRef]
220. Marola, S.; Bosia, S.; Veltro, A.; Fiore, G.; Manfredi, D.; Lombardi, M.; Amato, G.; Baricco, M.; Battezzati, L. Residual stresses in additively manufactured AlSi10Mg: Raman spectroscopy and X-ray diffraction analysis. *Mater. Des.* **2021**, *202*, 109550. [CrossRef]
221. Mukherjee, S.; Benavidez, E.; Crumb, M.; Calta, N.P. An Electrical Resistance Diagnostic for Conductivity Monitoring in Laser Powder Bed Fusion. *Sensors* **2024**, *24*, 523. [CrossRef]
222. Sen-Britain, S.T.; Keilbart, N.D.; Kweon, K.E.; Pham, T.A.; Orme, C.A.; Wood, B.C.; Nelson, A.J. *Chapter 5. Characterization of Surface Oxide Chemistry of New and Recycled Ti-Al Alloy Powders Used in Laser Powder Bed Fusion Additive Manufacturing*; Lawrence Livermore National Laboratory: Livermore, CA, USA, 2020; LLNL-TH-812982.
223. Freitas, B.J.M.; Koga, G.Y.; Arneitz, S.; Bolfarini, C.; Amancio-Filho, S.d.T. Optimizing LPBF-parameters by Box-Behnken design for printing crack-free and dense high-boron alloyed stainless steel parts. *Addit. Manuf. Lett.* **2024**, *9*, 100206. [CrossRef]
224. Ghauri, H.; Tafreshi, R.; Mansoor, B. Toward automated microstructure characterization of stainless steels through machine learning-based analysis of replication micrographs. *J. Mater. Sci. Mater. Eng.* **2024**, *19*, 4. [CrossRef]
225. Bai, Q.; Wu, B.; Qiu, X.; Zhang, B.; Chen, J. Experimental study on additive/subtractive hybrid manufacturing of 6511 steel: Process optimization and machining characteristics. *Int. J. Adv. Manuf. Technol.* **2020**, *108*, 1389–1398. [CrossRef]
226. Escalante-Quiceno, A.T.; Novotný, O.; Neuman, J.; Magén, C.; De Teresa, J.M. Long-Term Performance of Magnetic Force Microscopy Tips Grown by Focused Electron Beam Induced Deposition. *Sensors* **2023**, *23*, 2879. [CrossRef] [PubMed]
227. Hoffman, B.; Houbertz, R.; Hartmann, U. Eddy current microscopy. *Appl. Phys. A.* **1998**, *66*, S409–S413. [CrossRef]
228. Sophian, A.; Tian, G.Y.; Taylor, D.; Rudlin, J. Flaw detection and quantification for ferromagnetic steels using pulsed eddy current techniques and magnetization. *WIT Trans. Eng. Sci.* **2003**, *44*, 10. [CrossRef]
229. Staub, A.; Scherer, M.; Zehnder, P.; Spierings, A.B.; Wegener, K. Residual Stresses Measurements in Laser Powder Bed Fusion Using Barkhausen Noise Analysis. *Materials* **2022**, *15*, 2676. [CrossRef] [PubMed]
230. Plessis, A.D.; MacDonald, E.; Waller, J.M.; Berto, F. Non-destructive testing of parts produced by laser powder bed fusion. In *Fundamentals of Laser Powder Bed Fusion of Metals*; Elsevier: Amsterdam, The Netherlands, 2021; pp. 277–300. [CrossRef]
231. Silva, M.I.; Malitckii, E.; Santos, T.G.; Vilaça, P. Review of conventional and advanced non-destructive testing techniques for detection and characterization of small-scale defects. *Prog. Mater. Sci.* **2023**, *138*, 101155. [CrossRef]
232. Jeong, S.G.; Ahn, S.Y.; Kim, E.S.; Kang, S.H.; Yoo, S.H.; Ryu, J.Y.; Chun, J.H.; Karthik, G.M.; Kim, H.S. Liquation cracking in laser powder bed fusion-fabricated Inconel718 of as-built, stress-relieved, and hot isostatic pressed conditions. *Mater. Sci. Eng. A.* **2023**, *88*, 145797. [CrossRef]